

國立臺灣大學理學院大氣科學所

碩士論文

Graduate Institute of Atmospheric Sciences

College of Sciences

National Taiwan University

Master Thesis

季內振盪發展與熱帶波動、濕化、對流輻射過程之診
斷分析

A Diagnostic Study of the Evolution of the MJO Main-
tained by Wave Dynamics, Moistening and Convective-
Radiative Processes

洪竟書

Ching-Shu Hung

指導教授：隋中興 博士

Advisor: Chung-Hsiung Sui, Ph.D.

中華民國 105 年 6 月

June 2016



國立臺灣大學碩士學位論文 口試委員會審定書

本論文係洪竟書君（學號 R03229004）在國立臺灣大學大氣科學學系、所完成之碩士學位論文，於民國 105 年 6 月 13 日承下列考試委員審查通過及口試及格，特此證明

口試委員：

隋中興

（簽名）

（指導教授）

楊明仁

陳維序

系主任、所長

游政宏（簽名）

摘要



本研究利用ERA-Interim再分析與衛星觀測資料診斷低層水氣與整層濕靜能收支，以探討濕化過程與對流輻射反饋過程在季內振盪不同相位所扮演角色，並著重比較印度洋與海洋大陸之區域差異。為進一步探討前一個季內振盪的存在對下一個季內振盪生成與東移之影響，本研究進一步將季內振盪區分為successive與primary兩種類型，在1982-2011年北半球冬季期間分別挑選出22與5個東移訊號明顯的強季內振盪。研究結果顯示前一個季內振盪對流抑制區所引發之水氣平流與增強之輻射冷卻使環境之不穩定度增加，提供有利於下一個季內振盪對流發展之條件。

更進一步將successive類型的季內振盪生命期分成四個階段：對流抑制相位、對流成長相位、對流相位、對流消散相位。在對流抑制相位，大尺度沉降運動抑制對流發展高度，此時非降水性淺對流扮演水氣垂直傳送的角色，透過再蒸發將邊層水氣往中低對流層傳送，提供有利對流發展之環境。另外，前一個季內振盪對流抑制區所產生之季內尺度東風將暖池區較濕的空氣帶往印度洋，有利於對流在印度洋生成。在對流成長相位，主要之濕化過程除上述之東風水氣濕平流外，還有對流中心東側因邊界層磨擦產生之水氣輻合，兩者在對流區與其東側提供不穩定度，有利對流成長與東移。在對流相位，對流區潛熱釋放所產生之季內尺度西風與Rossby環流將西印度洋與熱帶外較乾之空氣帶入熱帶印度洋，使大氣變乾不利對流發展；對流區強降水為另一有效將水氣從大氣移除之機制。此時，前一個季內振盪對流抑制區東移至海洋大陸，其西側(對流區之東側)往兩極之Rossby環流將赤道地區較濕之水氣往南北兩側傳送，濕化對流區東側大氣，有利季內振盪由印度洋傳至海洋大陸。在對流消散相位，季內尺度西風增強，其水氣乾平流使對流逐漸消散。整體而言，海洋大陸地區主要之濕化過程與印度洋一致，惟在海洋大陸南北向水氣平流之重要性提升。

整層濕靜能收支診斷顯示，季內尺度輻射變化主要由長波輻射隨雲量與雲高

之變化主導，對流相位減弱之輻射冷卻增加整層濕靜能，有利於季內尺度濕靜能之維持。對流消散相位增強之西風與熱帶印度洋背景西風同向，增強海表蒸發，此為另一維持季內尺度濕靜能之過程。



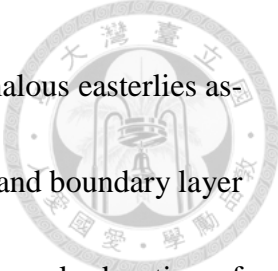
關鍵字：季內振盪、熱帶波動、濕化過程、對流輻射反饋過程、尺度分離

Abstract



The moistening processes for the Madden-Julian Oscillation (MJO) over Indian Ocean and Maritime Continent are investigated through a diagnosis of ECMWF Re-analysis (ERA-Interim) data in November-April, 1982-2011. During this period, 27 MJO events with strong magnitude and clear propagation are identified and further classified as either successive or primary, according to the existence of preceding events. The successive events are analyzed in the current study, whereas the primary events will be explored individually next.

A composite of scale-separated lower-tropospheric (1000-700 hPa) moisture (q_L) budget is analyzed in four stages: suppressed, cloud developing, convective, and decaying, each corresponding to the MJO Bimodal index phase 567, 81, 2, and 34 for Indian Ocean and 781, 23, 4, 56 for Maritime Continent, respectively. In the suppressed stage, the dominant moisture source over both region is surface evaporation/shallow convection ($-Q_2$), which is largely balanced by vertical dry advection. The advection of mean moisture by anomalous easterlies induced by the dry anomaly of previous events is another moistening process destabilizing the atmosphere over IO. Nonlinear zonal (meridional) advection by synoptic disturbances also has non-negligible contribution over IO (MC). In the cloud developing stage, q_L approaches maximum with moistening tendency to its east. This



moistening is contributed by the advection of mean moisture by anomalous easterlies associated with downstream Rossby wave response of the dry anomaly and boundary layer frictional moisture convergence. In the convective stage, while the zonal advection of anomalous westerlies and intense precipitation dries the atmosphere, the moistening of meridional advection by downstream Rossby anti-cyclonic gyres leads to the eastward propagation of deep convection. In the decaying stage, the strong westerlies bring in dry air from the west causing widespread drying. Overall, the moisture evolution of MC is consistent with IO except meridional component is more essential in suppressed stage.

A column-integrated moist static energy (MSE) budget is also analyzed to further identify the role of radiation and surface turbulent fluxes. The result shows that longwave heating is the dominant term in convective stage and latent heat flux is more prominent in decaying stage when the westerly is strong. The in-phase relation of longwave heating with column-integrated MSE suggests that longwave heating acts to maintain MSE and retard the propagation. Latent heat flux also slows down the propagation due to the phase lag.

Key words: Madden-Julian Oscillation 、 tropical wave dynamics 、 moistening 、 convective-radiative feedback 、 scale separation

Contents



口試委員審定書	i
摘要	ii
Abstract	iv
Contents.....	vi
Figure captions.....	viii
Table captions.....	xi
1. Introduction	12
2. Data and Methods.....	17
<i>a. Data</i>	<i>17</i>
<i>b. Bimodal ISO indices: the MJO and BSISO mode.....</i>	<i>18</i>
<i>c. Successive and primary events</i>	<i>19</i>
<i>d. Scale-separated moisture and MSE budget</i>	<i>21</i>
3. Composite result of successive MJO events	23
<i>a. Large-scale environment and MJO overall evolution</i>	<i>23</i>
<i>b. Low-tropospheric moisture budget</i>	<i>26</i>
<i>c. Column-integrated MSE budget</i>	<i>30</i>
4. Conclusion and discussion	33
References.....	37

Tables	42
Figures	43
Appendix	67

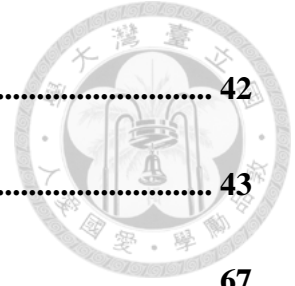




Figure captions

FIG. 1. The EOF patterns of the 25-90 day filtered OLR during (a) boreal winter (DJF) and (b) boreal summer (JJA). The number in the brackets shows the contribution of each EOF mode to total variance. The OLR values are multiplied by one standard deviation of the corresponding principal components to obtain the typical value and unit ($W m^{-2}$) for intraseasonal oscillations..... 43

FIG. 2. The composite life cycle of the MJO mode. The 20-60 day filtered OLR (shading, $W m^{-2}$) and horizontal wind fields at 850 hPa (vector, $m s^{-1}$)..... 44

FIG. 3. As in Fig. 2, except for the BSISO mode. 45

FIG. 4. Average number of days during which significant ISO (amplitude ≥ 1) is present in a month. The days are normalized such that they are the ratio of the number of days classified as the significant MJO mode (upper, blue) or significant BSISO mode (lower, red) to the number of days during 1982–2011 times the number of days in the month of common year..... 46

FIG. 5. The duration and corresponding bimodal phases for each selected MJO (blue) and BSISO (red) event in 1982-2011. The successive (primary) events are presented in dark (light) color. The width of the line and the font size of phase number denote the strength of the events. The gray vertical lines mark the transitional months, i.e., May and November..... 47

FIG. 6. (a) Hovmöller diagram of $10^{\circ}S$ - $10^{\circ}N$ averaged, 20-60 day filtered OLR (shading, $W m^{-2}$) and low-level zonal winds (contours, interval of $1 m s^{-1}$) for a successive event with a 101-day period (day 0 ± 50 days) from 15 February 1990 to 26 May 1990. Day 0 is defined as the day when OLR over Indian Ocean reaches minimum. (c) The corresponding phase diagram. The first ($t = -50$), central ($t = 0$), and last ($t = 50$) days are denoted by a filled circle, a filled diamond, and a filled square, respectively. (b) and (d) are as (a) and (c), expect for a primary event with a 101-day period from 10 December 2000 to 20 March 2001. The text N denotes the region where the amplitude is smaller than 1. See text for details. 48

FIG. 7. (a) 1000-700 hPa integrated low-frequency moisture (shading, $g kg^{-1}$) and wind fields (vector, $m s^{-1}$) and (b) standard deviation of 20-60 day filtered OLR (shading, $W m^{-2}$) and seasonal mean precipitation (contours, $mm day^{-1}$) during

boreal winter. The purple boxes marks the locations of four MJO activity centers in sequence from the left side to the right: WIO (15°S-5°N, 45°E-65°E), CIO (10°S-10°N, 70°E-90°E), MC (12.5°S-7.5°N, 100°E-155°E), and WP (12.5°S-7.5°N, 100°E-155°E). 49

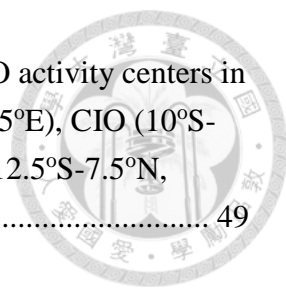


FIG. 8. Composit ed Hovmöller diagram of 10°S-10°N averaged, 20-60 day filtered OLR (shading, $W m^{-2}$) and low-level zonal winds (contours, interval of $1 m s^{-1}$). The purple solid (dashed) lines mark the location of OLR maximum (minimum). The red D indicates the positive OLR anomaly associated with previous events. . 50

FIG. 9. Composit ed Hovmöller diagram of 10°S-10°N averaged, 20-60 day filtered OLR (shading, $W m^{-2}$) and low-tropospheric moisture (contours, interval of $10^6 J m^{-2}$; L is absorbed into q). The purple solid (dashed) lines mark the location of OLR maximum (minimum). 51

FIG. 10. Composit ed zonal-vertical distribution of 10°S-10°N averaged, 20-60 day filtered moisture (shading, interval of $10^2 J kg^{-1}$; L is absorbed into q) in eight MJO bimodal index phases. 52

FIG. 11. (a) Time series of 20-60 day OLR anomaly (green solid line) and low-tropospheric moistures (blue dashed line) over Central Indian Ocean. Suppressed (red), cloud developing (blue), convective (green), and decaying (pink) stages are shaded. The day 0 in this figure represent the day when the OLR anomaly turns negative. The numbers above the x axis are the corresponding MJO bimodal index phase. (b) is as (a), expect for Maritime Continent. 53

FIG. 12. Vertical structure of 20-60 day filtered (a) moisture, (b) MSE, (c) pressure velocity, and (d) zonal winds over Central Indian Ocean in four stages (suppressed in red, cloud developing in blue dashed, convective in green, and decaying in pink dashed). (e)-(h) are as (a)-(d), expect for Maritime Continent. 54

FIG. 13. Composit ed Hovmöller diagram of 10°S-10°N averaged, 20-60 day filtered low-tropospheric moisture budget terms (shading, $W m^{-2}$): (a) tendency, (b) $-Q_2$, (c) horizontal advection, and (d) vertical advection. Budget terms are shown only when they are statistically significant at 95% confidence level. Contoured in each panel is low-tropospheric moisture ($J m^{-2}$) anomaly with interval of $10^6 J m^{-2}$. The purple solid (dashed) lines mark the location of OLR maximum (minimum). 55

FIG. 14. As in Fig. 13, expect for (a) zonal advection and (b) meridional advection term. Contoured in each panel is low-tropospheric moisture (J m^{-2}) anomaly with interval of 10^6 J m^{-2} . The purple solid (dashed) lines mark the location of OLR maximum (minimum).....	56
FIG. 16. As in Fig. 15, expect for Maritime Continent.....	58
FIG. 17. (a) 20-60 day filtered OLR (shading, W m^{-2}) and low-level winds (vector, m s^{-1}); Horizontal distribution of low-tropospheric moisture budget terms (shading, W m^{-2}) during the CIO suppressed stage: (b) $\omega \partial q / \partial p - Q_2$, (c) tendency, (d) vertical advection, (e) horizontal advection, (f) $-Q_2$. Contoured in each panel is the low-tropospheric moisture (J m^{-2}) anomaly with interval of 10^6 J m^{-2} . (g) $-u_2 \partial q / \partial x$, (h) $-v_2 \partial q / \partial y$ and 20-60 day filtered low-level winds (vector, m s^{-1}).....	59
FIG. 18. As in Fig. 17, except for CIO cloud developing stage.	60
FIG. 19. As in Fig. 17, except for CIO convective stage.	61
FIG. 20. As in Fig. 17, except for CIO decaying stage.	62
FIG. 21. As in Fig. 17, except for MC suppressed stage.	63
FIG. 22. (a) Column-integrated MSE budget terms and (b) the decomposition of $Q_1 - Q_2$ averaged over four stages. 95% statistically significant budget terms are shown in red. The error bar presents the standard deviation of each term.....	64
FIG. 23. As in Fig. 22, except for Maritime Continent.	65
FIG. 24. Horizontal distribution of column-integrated MSE budget terms (shading, W m^{-2}) during the CIO convective stage: (a) tendency, (b) vertical advection, (c) horizontal advection, (d) $Q_1 - Q_2$. Contoured in each panel is the column-integrated MSE anomaly with interval of 10^6 J m^{-2} . The decomposition of $Q_1 - Q_2$: (e) longwave radiation, (f) shortwave radiation, (g) latent heat flux, and (h) sensible heat flux. The red (blue) vectors in (g) denote the regions where the intraseasonal flows are in the same (opposite) direction to mean flows.	66



Table captions

Table 1. Number of days for each of the four categories. The number in the brackets shows the ratio to the total number of days (10957 days) during 1982-2011. 42

Table 2. Number of instances of the successive and primary events for ISO (left). Number of consecutive events for ISO (right). Single means there is no consecutive event (DABCD), double indicates a continuation of two events (DABCDABCD), and so forth. 42

Table 3. The low-level moisture budget of four stages over the Central Indian Ocean. 95% statistically significant budget terms are shown in boldface. 42

Table 4. As in Table 3, expect for Maritime Continent. 42

Table A1. Number of days for each of the four categories as in Table 1. The number in the brackets shows the ratio to the total number of days (10957 days) during 1982-2011. 68

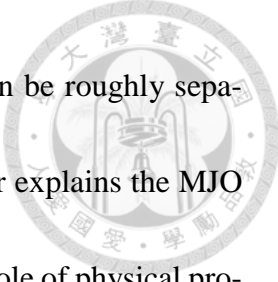
Table A2. Number of instances of the successive and primary events for ISO (left) as in Table 2. Number of consecutive events for ISO (right) as in Table 2. Single means there is no consecutive event (DABCD), double indicates a continuation of two events (DABCDABCD), and so forth. 68



1. Introduction

The Madden-Julian Oscillation is the dominant intraseasonal variability in the tropical atmosphere. It can be described as a tropical planetary-scale circulation system coupled with a multi-scale convective complex and propagating eastward slowly with a rearward tilted vertical structure and a mixed Kelvin-Rossby wave horizontal structure (Madden and Julian 1972; Wheeler and Kiladis 1999; Wheeler et al. 2000; Kiladis et al. 2005; Wang 2011). The planetary-scale circulation anomalies associated with the MJO significantly modulate the tropical weather, such as monsoon onset, tropical cyclone genesis, and ENSO development. Through tropical-extratropical teleconnections, it can influence the mid-latitude weather as well. Therefore, understanding the dynamics of the MJO is important for the diagnosis and prediction of global weather and climate. However, the state-of-art general circulation models (GCMs) still simulate the MJO with an unsatisfactory skill and recent studies have shown that there is a gap of 20–25 days between the potential and practical predictability of the MJO (Kim et al. 2014; Neena et al. 2014). In order to improve MJO simulation and advance the medium-range predictability, a better understanding of the fundamental processes driving MJO dynamics (e.g., the slow eastward propagation, intraseasonal time scale, and planetary zonal scale) is required.


A variety of theories have been proposed to explain the growth and propagation




mechanism of MJO. Based on their key feedback processes, they can be roughly separated into two categories: dynamics and thermodynamics. The former explains the MJO by forced tropical wave dynamics, whereas the latter emphasizes the role of physical processes (e.g., moistening, surface turbulent fluxes, and radiative fluxes).

In the wave dynamics theories, the MJO is first interpreted as viscous Kelvin waves by Chang (1977) and further elaborated by Lau and Peng (1987) as moist Kelvin-Rossby waves with an instability arising from the interaction between convective heating and large-scale wave motion, known as wave CISK. This convective-coupling reduces the effective static stability and thus slows down the propagation speed of Kelvin wave ($\sim 19 \text{ m s}^{-1}$). The intraseasonal period of MJO is determined by the time needed for the moist Kelvin wave to circumnavigate the globe. However, the moist Kelvin wave speed is still significantly faster than the observed MJO propagation speed ($\sim 5 \text{ m s}^{-1}$) and the mode is most unstable in small wavelength, which is opposite to the planetary zonal scale of observed MJO. To solve these problems, Wang and Li (1994) introduced a boundary layer into the traditional wave-CISK model framework. The heating associated with the boundary layer frictional-induced convergence (FC) ahead of the free tropospheric wave convergence can couple the Kelvin and Rossby waves together and select a slow eastward propagation with a planetary zonal scale (Wang and Chen 2016, submitted).

Recently, the second set of theories have received more attention in explaining the

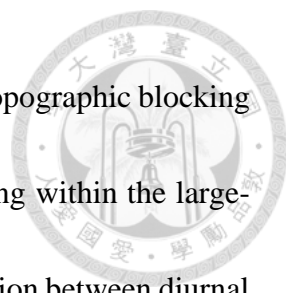


observed feature of MJO, such as the recharge-discharge theory (Bladé and Hartmann 1993; Hu and Randall 1994; Kemball-Cook and Weare 2001; Stephens et al. 2004; Benedict and Randall 2007), the wind-evaporation feedback (Emanuel 1987), the cloud-radiative feedback (Hu and Randall 1994; Anderson and Kuang 2012), and the moisture mode theory (Sobel and Maloney 2012, 2013; Adames and Kim 2016). Several observational studies have shown that the development and propagation of MJO are closely related to the atmospheric moisture, radiation, and surface turbulent fluxes (Sobel et al. 2014; Johnson et al. 2015; Tseng et al. 2015). The MJO simulations in some GCMs are also improved when convection is made more sensitive to environmental moisture (Hannah and Maloney 2011) and become weaker when cloud-radiative interaction is turned off (Anderson and Kuang 2012). Since the physical processes (e.g., moistening, turbulent fluxes, and radiation) emphasized by these theories act as the energy sources of moist static energy (MSE) and will modulate the local convective instability, they can be all integrated into the recharge-discharge framework. The one-dimensional modeling study of Hu and Randall (1994) has shown that the interactions among radiation, convection, and turbulent fluxes can set up an oscillating diabatic heat source with a period similar to that of the observed MJO. The timescale of the oscillation is determined by the recharge and discharge time for the local instability. This gradual buildup of local instability consists well



with the cloud evolution of MJO from shallow cumuli and congestus cloud to deep convection (Benedict and Randall 2007). Through the diagnosis of moisture and MSE budget, some key processes contributing to the evolution of local instability are identified. While the horizontal and vertical moisture advection are responsible for the eastward propagation, the growth and maintenance are associated with the radiation and surface turbulent fluxes (Sobel et al. 2014; Tseng et al. 2015; Kerns and Chen 2014; Kim et al. 2014; Zhao et al. 2013; Hsu and Li 2012).

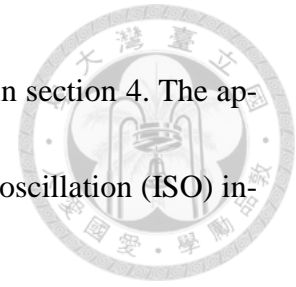
Although many studies have discussed the role of moisture, radiation, and turbulent fluxes to the development and propagation of MJO, most of them focus on the Indian Ocean region, where the MJO initiates and starts propagating eastward, within a short period. Yet, the eastward propagation is not smooth with the strength of convection changing from locations. For a typical MJO life cycle, the convective envelopes initiate from the western Indian Ocean, strengthen over the center Indian Ocean, bifurcate while passing through the Maritime Continent, reintensify upon reaching the west Pacific, and finally dissipate around date line. Thus, the results obtained from Indian Ocean may not be the same for other regions, especially for the Maritime Continent. The complex topography and land-sea contrast over that region strongly modulate the MJO convective envelopes as they pass through. Wu and Hsu (2009) suggests that the distribution of mountainous islands seems to result in the southward detour of the eastward-propagating MJO



and the sudden shift of deep convection between major islands. The topographic blocking and mountain wave-making effect will create extra lifting and sinking within the large-scale circulation of MJO. Peatman et al. (2014) found that the interaction between diurnal cycle and MJO leads to the vanguard of precipitation jumping ahead of the main MJO convective envelopes by 6 days (~one phase). Moreover, some other studies suggest that the circulation of preceding MJO events may help to generate the next MJO (Matthews 2008; Kim et al. 2014; Zhao et al. 2013) and the model prediction skill of MJO is also better when the forecasts are initialized with strong MJOs compared to those initialized with weak or nonexistent MJOs (Kim et al. 2014). Therefore, the identification of individual attribution from current and previous events is crucial to advance our understanding for the initiation and propagation mechanism of MJO and improve model prediction skills.

Based on previous research, this study aims to investigate the relative contribution of large-scale wave dynamics and local physical processes (e.g., low-tropospheric moistening, radiation, and surface turbulent fluxes) to the initiation and propagation under different type of MJO events, i.e., successive and primary (Matthews 2008), over different regions with 30-year reanalysis data. The remainder of this article is organized as follows. Section 2 describes the data and methods of analysis employed in this study. In section 3, the evolution of composite successive MJO events is discussed through the diagnosis of

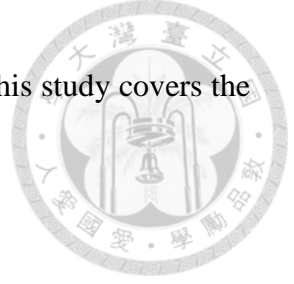
moisture and MSE budget. Finally, concluding remarks are offered in section 4. The appendix present an intercomparison of some traditional intraseasonal oscillation (ISO) indices with the bimodal ISO indices utilized in this study.



2. Data and Methods

a. Data

The datasets used in this study include 1) the interpolated daily outgoing longwave radiation (OLR) obtained from National Oceanic and Atmospheric Administration (NOAA) polar-orbiting satellites (Liebmann and Smith 1996) and 2) the ERA-Interim reanalysis data from the European Centre for Medium-Range Weather Forecasts (ECMWF). The OLR data is used to represent the deep convection and identify significant intraseasonal oscillation (ISO) events. It has a horizontal resolution of $2.5^\circ \times 2.5^\circ$, with temporal resolution of 1 day. The ERA-Interim data is utilized to diagnose the moisture and MSE budget and describe the overall structure of ISO. It contains zonal and meridional winds, vertical p velocity, geopotential and specific humidity at 15 levels from 1000 to 100 hPa. In addition, the surface product is used to estimate the boundary fluxes at the surface and top of atmosphere (e.g., longwave/ shortwave radiative flux and surface latent/sensible heat flux). To unify the resolutions among datasets, the 6-hourly 1.5° ERA-




Interim data is interpolated into daily and 2.5° grid. The analysis in this study covers the period from 1982 to 2011.

b. Bimodal ISO indices: the MJO and BSISO mode

Given the observational evidence that the ISO shows distinct behaviors between two solstice seasons, the traditional all-season real-time multivariate MJO (RMM) index (Wheeler and Hendon 2004) may not resolve the regional features of the annual variation for ISO properly (e.g., Lee et al. 2013). Thus, the method developed by Kikuchi et al. (2012) is adopted to construct the bimodal ISO indices, i.e., an EOF analysis is performed on the 25-90 day FFT-filtered OLR during the boreal winter (DJF) and summer (JJA), respectively. The leading EOF modes (Fig. 1):

$$OLR_{mode}(t) = EOF_{1,mode} \times PC_{1,mode} + EOF_{2,mode} \times PC_{2,mode} \quad (1)$$

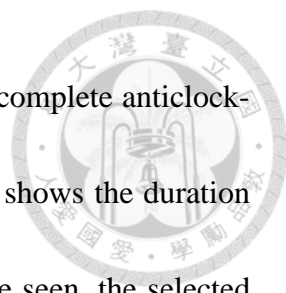
derived from the winter and summer season are respectively defined as the Madden Julian Oscillation (MJO) mode [$EOF_{1,MJO}$, $EOF_{2,MJO}$] and the boreal summer intraseasonal oscillation (BSISO) mode [$EOF_{1,BSISO}$, $EOF_{2,BSISO}$]. The corresponding normalized PCs [$PC_{1,mode}^*$, $PC_{2,mode}^*$] of the MJO and BSISO mode then form the bimodal ISO indices similar to the RMM index. The composite eight-phase life cycle (Fig. 2 and 3) and seasonal distribution (Fig. 4) of the two modes are in good agreement with Kikuchi et al. (2012). While the MJO mode shows a predominant eastward propagation along the equator with a southward detour over MC region during December to April, the BSISO mode



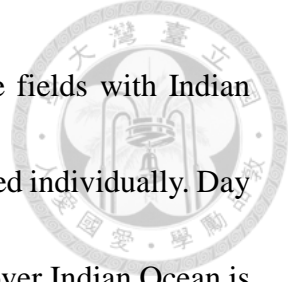
has a prominent northward propagation in off-equatorial monsoon trough regions during June to October. Comparing with the RMM index derived from all-season data (Fig. 8 and Fig. 9 in Wheeler and Hendon 2004), the bimodal indices can capture more distinct off-equatorial structures, especially for the northward propagation during boreal summer. May and November are the transitional months with comparable magnitude between MJO and BSISO (Fig. 4). In the current study, we focus on the boreal winter MJO mode only.

c. Successive and primary events

Since some conventional analyses of MJO (e.g., lag regression method) tend to produce a repeating MJO cycle, it is difficult to separate the individual attribution from current and previous events. Matthews (2008) utilized the phase diagram of OLR-only MJO index to divide the MJO life cycle into four categories. Category A contains the traditional RMM phase 2 and 3, category B includes phase 4 and 5, and so forth. Days with amplitude ($A = \sqrt{PC_1^* + PC_2^*}$) below the critical value ($A_c = 0.4$) were assigned to a category N (no MJO). The primary MJO events with no preceding cycle of MJO are defined as NABCD, while the successive MJO events following on from a previous cycle of MJO are defined as DABCD. We then extend this case selection method to the bimodal ISO indices derived above to identify both MJO and BSISO events. Based on the bimodal ISO index of MJO (BISISO) mode with A_c set at 1, 22 (23) successive and 5 (8) primary events with strong



magnitude, i.e., amplitude larger than 1, and clear propagation, i.e., complete anticlockwise circuit, are selected in the period of interest 1982-2011. Fig. 5 shows the duration and corresponding bimodal phases of each selected event. As can be seen, the selected MJO and BSISO events dominate over the boreal winter and summer respectively. It is noticeable that the primary events, both MJO and BSISO, often occur in the transitional months. Examples for successive and primary events are presented in Fig. 6. The successive event has clear eastward propagating anomalies prior to its initiation, whereas the primary event has no coherent signal before initiation. The detail statistics of the selected events are presented in Table 1 and 2. The results in Table 1 show that less than one-fourth of the year has significant ISO signal and the signal is weakest over Maritime Continent region (category B). The 77% (45/58) successive to total event ratio shown in Table 2 is slightly higher than the 60% (26/82) obtained by Matthews (2008) and lower than the 80% obtained from the model simulation (Maloney and Wolding 2015). The discrepancy with Matthews (2008) may result from the different choice of critical value (0.4 and 1) and the use of bimodal indices in our method could reduce the selected amount of primary events in the transitional months. The high successive ratio in the model simulation suggests that the dynamics of MJO initiation in the model are dominated by interactions with preceding events. A more detailed comparison of the selected ISO events, as revealed by other ISO indices (e.g., RMM index), is presented in appendix.



In this study, the successive events are analyzed in composite fields with Indian Ocean OLR minimum as day 0, and the primary events will be explored individually. Day 0 in each event represents the day when the 25-90 day filtered OLR over Indian Ocean is minimum.

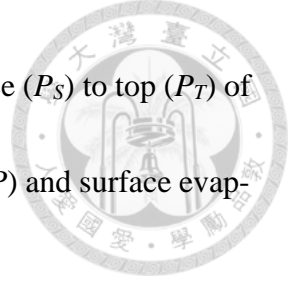
d. Scale-separated moisture and MSE budget

The budget analysis of the major MJO events is performed based on the ERA- interim reanalysis data. To further examine the contribution of the non-linear scale interaction to intraseasonal variability, a scale-separated low-tropospheric moisture budget is calculated by decomposing moisture (q) and winds (u, v, ω) into three components [$a = a_1 + a_2 + a_3$; a_1, a_2 , and a_3 denote low-frequency (>60 days), MJO (20-60 days), and high-frequency (<20 days) bands, respectively] and all components contributing to MJO scale moisture tendency are estimated by

$$\left[\frac{\partial q}{\partial t} \right]' = - \left[u \frac{\partial q}{\partial x} \right]' - \left[v \frac{\partial q}{\partial y} \right]' - \left[\omega \frac{\partial q}{\partial p} \right]' - [Q_2/L]'. \quad (2)$$

Where the prime denotes the bandpass filtered at MJO scale and the square brackets denote vertical integration in the lower troposphere from surface to 700 hPa. Moisture (q) is represented in energy unit with L absorbed. The residual of the moisture budget, known as moisture sink (Q_2), includes the subgrid-scale contribution of condensation (c), evaporation (e), and eddy moisture flux convergence (Yanai et al. 1973),

$$Q_2 = L \left(c - e + \frac{\partial \overline{\omega^* q^*}}{\partial p} \right). \quad (3)$$



The column-integrated Q_2 , defined as vertical integration from surface (P_S) to top (P_T) of troposphere, represents the net moisture sink between precipitation (P) and surface evaporation (E),

$$\int_{P_T}^{P_S} Q_2 \frac{dp}{g} = L(P-E). \quad (4)$$

To further identify the role of radiation and surface turbulent fluxes, a column-integrated MSE budget is also analyzed by the equation below:

$$\left[\frac{\partial h}{\partial t} \right]' = - \left[u \frac{\partial h}{\partial x} \right]' - \left[v \frac{\partial h}{\partial y} \right]' - \left[\omega \frac{\partial h}{\partial p} \right]' + [Q_1 - Q_2]'. \quad (5)$$

The notation is the same as the moisture equation except that h denotes MSE,

$$h = C_p T + gz + Lq = s + Lq, \quad (6)$$

and the square brackets now denote vertical integration from surface to 100 hPa. The residual of the dry static energy (DSE) budget, known as apparent heat source (Q_1), includes the subgrid-scale contribution of condensation, evaporation, radiative heating (Q_R), and eddy DSE flux convergence (Yanai et al. 1973),

$$Q_1 \equiv \frac{\partial s}{\partial t} + u \frac{\partial s}{\partial x} + v \frac{\partial s}{\partial y} + \omega \frac{\partial s}{\partial p} = L(c-e) - \frac{\overline{\partial \omega^* s^*}}{\partial p} + Q_R. \quad (7)$$

The column-integrated Q_1 represents the net heating between precipitation, surface sensible heat flux (SH), longwave radiation (ΔLW), and shortwave radiation (ΔSW),

$$\int_{P_T}^{P_S} Q_1 \frac{dp}{g} = LP + SH + \Delta LW + \Delta SW. \quad (8)$$

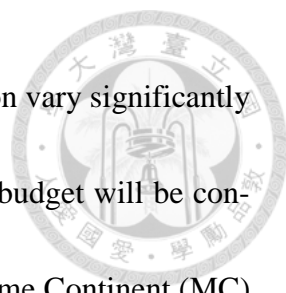


3. Composite result of successive MJO events

In this section, the evolution of successive MJO is explored based on the composite results of the 22 events selected.

a. Large-scale environment and MJO overall evolution

The low-frequency moistures and wind fields averaged over all composite days are shown in Fig. 7a. In the Indo-Pacific tropical region where the MJO is most active, moistures gradually increase eastward and off-equatorial easterlies converge equatorward and further turn into westerlies over the equatorial Indian Ocean. Those mean state features influence the evolution of MJO in different regions. To demonstrate the interaction between the mean state and intraseasonal variability, the mean precipitations during boreal winter are superimposed onto the variance of 20-60 day filtered OLR (Fig. 7b). The maximum MJO activity coincides with the seasonal mean precipitation zone, suggesting the large-scale control of the mean circulation on MJO. The result also shows a significant land-sea contrast with enhanced intraseasonal variance over the oceans and reduced variance over the lands, especially in the Maritime Continent. In these regions, the climatological precipitation maximizes over main islands (e.g., Sumatra, Borneo, and New Guinea), while intraseasonal variability is minimum. This feature may relate to the strong diurnal cycle there. Peatman et al. (2014) reports that 80% of the MJO precipitation signal over Maritime Continent is accounted for by changes in the amplitude of the diurnal cycle.



Since the MJO activity, mean state fields, and topographic distribution vary significantly in different longitudes, the detailed diagnosis of MJO structure and budget will be conducted respectively in the central Indian Ocean (CIO) and the Maritime Continent (MC) region as shown in Fig. 7b.

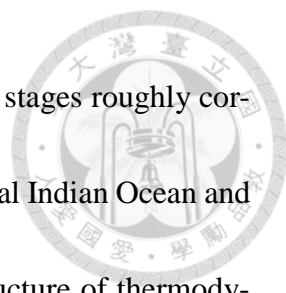
The overall evolution of the successive events is illustrated by the composited Hovmöller diagram of intraseasonal OLR anomaly and low-level zonal winds in Fig. 8. Two slowly eastward-propagating ($\sim 5 \text{ m s}^{-1}$) convective envelopes with one following the other are revealed. As will be discussed later, the suppressed convection of previous events (marked by the red D in Fig. 8) plays an important role in the initiation and propagation of subsequent events. Besides the eastward propagation, the geographic dependence is distinct. The large-scale convective envelopes initiate from the western Indian Ocean (WIO), strengthen over the central Indian Ocean (CIO), weaken while passing through the Maritime Continent (MC), reintensify upon reaching the west Pacific (WP), and finally dissipate around date line due to the cold SST there. While the convection dissipates, the wind signals continue propagating eastward around the globe with a much faster speed ($\sim 20 \text{ m s}^{-1}$). Some studies hypothesize that this circumnavigating signal excited by previous MJO will trigger another MJO once it reached the Indian Ocean. However, it is still unclear how the zonal wind anomalies would trigger MJO convection. Recently, the effect of previous MJO event on triggering next MJO focuses on the moisture

advection of downstream Rossby wave response to preceding suppressed convection (Zhao et al. 2013; Kim et al. 2014), as discussed in this study.



The MJO moisture-convection relationship is illustrated in Fig. 9. As shown in Fig. 9, 10 days prior to the initiation of convection over the WIO (day -15), the 1000-700 hPa integrated specific humidity anomalies begin to increase. This buildup of moisture in the lower troposphere destabilizes the atmosphere and thus generates a favorable environment for potential development of convection. Following the initial development over WIO, the enhanced (suppressed) low-level moisture to the east (west) of the MJO convective center leads to the eastward propagation (Hsu and Li 2012). This zonal asymmetry of low-level moistures is illustrated more clearly in the zonal-vertical distribution shown in Fig. 10. During phase 2 (convection is strongest over Indian Ocean), while the maximum moisture anomalies in the middle troposphere are collocated with the Indian Ocean convection, the low-level moistures have increased over Maritime Continent. This low-level buildup to the east of convection center can be seen in all phases of MJO life cycle.

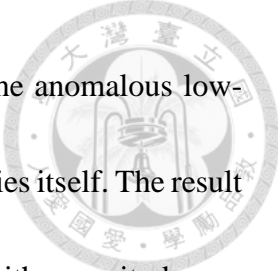
Following the definition proposed by Tseng et al. (2015), the MJO life cycle is separated into four stages based on the evolution of OLR anomaly and low-level moisture: suppressed (OLR' is positive and $[q]'$ is low), cloud developing (OLR' turns negative and $[q]'$ grows to a maximum), convective (OLR' reaches maximum) and decaying (OLR'



increases and $[q]'$ decreases). As displayed in Fig. 11, the above four stages roughly correspond to the MJO Bimodal index phase 567, 81, 2, and 34 for Central Indian Ocean and 781, 23, 4, 56 for Maritime Continent, respectively. The vertical structure of thermodynamic and dynamic fields during four stages are shown in Fig. 12. In the suppressed stage, the intraseasonal downward motion causes the strong drying in the middle troposphere and the easterlies induced by the Rossby wave response of suppressed convection prevail over low troposphere. In the cloud developing stage, the low-level moistures build up and increase the instability. Convection begins to develop and change the environment into upward motion. In the convective stage, the middle troposphere moistens and the strong upward motion peak at 300-400 hPa. The low-level westerlies induced by the convective heating also establish. In the decaying stage, the low-level moistures start decreasing and the low-level westerlies become stronger. Generally, the vertical structure over Maritime Continent is consistent with Indian Ocean, both showing a low-level moisture buildup and a first baroclinic wind structure. Moreover, since the strength of convective instability can be represented by the change of the vertical structure of MSE, the resemblance between the moisture and MSE anomalies suggests that moisture is the main factor controlling the intraseasonal evolution of convective instability.

b. Low-tropospheric moisture budget

Given the importance of low-tropospheric moisture to the MJO evolution, a 1000-



700 hPa integrated moisture budget is performed. Fig. 13 exhibits the anomalous low-tropospheric moisture budget terms together with the moisture anomalies itself. The result shows that the vertical advection and $-Q_2$ are the dominant terms with magnitude one order larger than the tendency and horizontal advection. However, since they are mostly out of phase and thus cancel each other, the overall evolution of tendency resembles that of the horizontal advection. The horizontal advection term has a prominent positive contribution around 100°E - 180° between negative and positive moisture anomaly, suggesting an important role of horizontal advection for the eastward propagation over the MC and WP. Moreover, there is positive horizontal advection over the IO when the moisture anomaly is positive. This in-phase relation would further amplify the moisture anomaly and contribute to the growth and maintenance of MJO convection. To identify the process responsible for the horizontal advection, the term is further decomposed into zonal and meridional parts in Fig. 14. The result shows that while the meridional advection dominates over the MC and WP region and mostly contributes to the eastward propagation, the zonal advection plays a more important role for the growth over the IO.

The influence of scale interaction on intraseasonal variability is investigated by the scale-separated budget described in section 2d. To determine the relative contribution of each budget term to the local moisture evolution in the specific region, the time series of each budget term over that region is projected to the time series of local tendency. It is

calculated as:

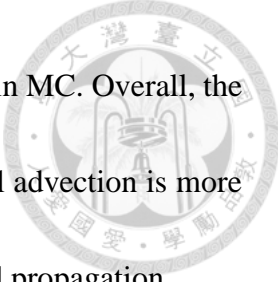
$$\frac{\langle f, \frac{\partial q_2}{\partial t} \rangle}{\langle \frac{\partial q_2}{\partial t}, \frac{\partial q_2}{\partial t} \rangle} \quad (9)$$



Where the f represents each budget term and the brackets denote inner product. Since the MJO is an eastward propagating weather system, the projection onto local tendency can be interpreted as the contribution to eastward propagation. The projections over CIO and MC are displayed in Fig. 15a and Fig. 16a. The result over IO shows that both horizontal and vertical advection have positive contribution to the tendency, while the contribution from the subgrid-scale processes ($-Q_2$) is negative. The leading term in the moisture advection, both horizontal and vertical, is the advection of mean moisture (q_1) by the MJO flow (U_2). Over MC region, the eastward propagation is dominated by the horizontal advection with insignificant contribution from the vertical advection and $-Q_2$. Nonlinear advection by synoptic disturbances ($q_3 U_3$) also has non-negligible contribution. The projection of each budget term onto moisture anomaly (q_2) is further calculated to evaluate its contribution to local moisture growth and maintenance (Fig. 15b and Fig. 16b). This is calculated in a similar way to the contribution to the propagation:

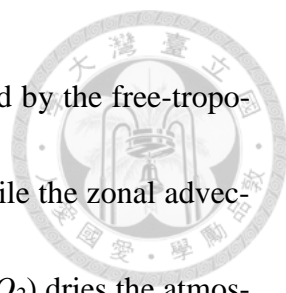
$$\frac{\langle f, q_2 \rangle}{\langle q_2, q_2 \rangle} \quad (10)$$

The results over both region show that the vertical advection by upward motion is the dominant moisture source and the intense precipitation ($-Q_2$) efficiently removes moisture




from atmosphere. Horizontal advection has a small contribution only in MC. Overall, the moisture evolution of MC is consistent with IO except that horizontal advection is more essential and the synoptic disturbances also contribute to the eastward propagation.

To better understand the processes resulting in the moisture change, the horizontal distribution of dominant budget terms is studied in the four stages as defined in section 3a. Fig. 17-20 exhibit the moisture budget terms over the CIO during four stages. For all stages, as the vertical advection and $-Q_2$ largely cancel each other, the horizontal pattern of tendency term resembles that of the horizontal advection. This result is consistent with the analysis of Hovmöller diagram. The detail features for each stage are discussed below. In the suppressed stage, the dominant moisture source is the surface evaporation/shallow convection ($-Q_2$), which is largely balanced by the vertical dry advection induced by intraseasonal downward motion of previous event (Fig. 17d). The net effect, termed as column processes in several studies (Chikira 2014; Wolding and Maloney 2015), illustrated in Fig. 17b has a positive contribution to the moistening tendency in the northern hemisphere over CIO. The zonal advection of mean moisture by anomalous easterlies associated with downstream Rossby wave response of the dry anomaly also contributes to the low-level moisture buildup (Fig. 17g). In the cloud developing stage, low-level moisture approaches maximum with a moistening tendency to its east (Fig. 18a). This moistening is mainly contributed by the advection of mean moisture by anomalous easterlies (Fig.



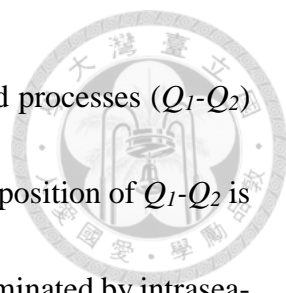
18g) and the boundary layer frictional moisture convergence induced by the free-tropospheric heating of main MJO (Fig. 18d). In the convective stage, while the zonal advection of anomalous westerlies and intense precipitation (i.e., positive Q_2) dries the atmosphere, the moistening caused by the strong intraseasonal upward motion largely counteracts their effects. The meridional advection by downstream Rossby anti-cyclonic gyres moistens the MC region and leads to the eastward propagation of deep convection. The off-equatorial position of this moistening may contribute to the southward detour of MJO when it passes through MC. In the decaying stage, the strong westerlies bring in dry air from the west causing widespread drying in CIO. Since the moisture evolution of MC is consistent with IO to first order, here only the results from selected stages are displayed (Fig. 21) to illustrate the difference between two regions. In the suppressed stage of MC, as the convection has developed over IO, its heating will induce boundary layer frictional moisture convergence to the east. This is an additional moistening process over MC that is not seen in the suppressed stage over IO. Moreover, the area-averaged moisture budgets over CIO and MC during four stages are presented in Table 3 and 4. Overall, the result of the MC is consistent with the IO except that the meridional component is more significant over MC.

c. Column-integrated MSE budget



Although the diagnosis of moisture budget has provided much insight into the initiation and propagation mechanism for MJO, the budget residual (Q_2) is one order larger than the individual terms that we identify as key processes, such as the horizontal advection. The small moisture tendency, which is important to the moisture evolution associated with MJO, is the result of a near balance between large values of vertical advection and budget residual. It is this large cancellation that makes it difficult to assess an accurate calculation of moisture budget. The use of MSE budget can partly alleviate this problem by canceling the dominant condensation term when adding the moisture and DSE equation. Moreover, as the radiation and surface turbulent fluxes are the source and sink in the column-integrated MSE budget, the role of these diabatic processes in the evolution of MJO can be explored explicitly.

The column-integrated MSE budget averaged over CIO during four stages are shown in Fig. 22 and their horizontal distributions during convective stage are displayed in Fig. 24. Since the weak temperature gradient (WTG) in the tropical region, the MSE tendency and horizontal advection term is consistent with the moisture budget analysis (Fig. 19). The main difference is the sign of the vertical advection as the column-integrated MSE vertical advection is dominated by upper-level geopotential energy. It is worth noting that the magnitude of vertical advection and the budget residual (Q_1-Q_2) are of the same order as the horizontal advection, since the largest term (i.e., precipitation) in the moisture



budget residual is canceled by the condensation heating. The subgrid processes (Q_1-Q_2) include the radiative heating and surface turbulent fluxes. The decomposition of Q_1-Q_2 is shown in Fig. 22b. The results show that the evolution of Q_1-Q_2 is dominated by intraseasonal variation of longwave radiation. The positive contribution of surface latent heat flux is only prominent during the decaying stage as the strong intraseasonal westerlies are in the same direction with the mean-state westerlies over equatorial Indian Ocean (Fig. 24g). The variation of shortwave radiation and surface sensible heat flux are small comparing to the other two terms. The detail features in each stage are discussed below. In the suppressed stage, the radiative cooling is enhanced due to the lack of deep convection and the intraseasonal easterlies against the mean winds reduce the surface latent heat flux. In the cloud developing stage, the gradual increases of cloud coverage and cloud height reduce the radiative cooling. In the convective stage, the widespread cloud coverage and elevated cloud top cause significant radiative heating. In the decaying stage, the prevailing stratiform clouds also reduce the radiative cooling and the strong intraseasonal westerlies enhance the surface latent heat flux.

The in-phase relation of longwave heating with column-integrated MSE in convective stage suggests that longwave heating acts to maintain MSE and the positive contribution in decaying stage retards the eastward propagation. Through wind-evaporation feedback, surface latent heat flux also slows down the propagation due to the phase lag

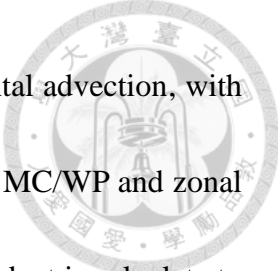
between convection and wind. The MSE budget analysis over Maritime Continent is also calculated (Fig. 23). To first order, the result is consistent with that over Indian Ocean.



4. Conclusion and discussion


In this study, 30-year ERA-Interim reanalysis data and NOAA OLR satellite observation are used to investigate the relative contribution of moistening, radiative heating, and turbulent fluxes to the initiation and propagation of MJO over Indian Ocean and Maritime Continent. The method developed by Kikuchi et al. (2012) is adopted to construct bimodal ISO indices that can capture the annual variation of intraseasonal oscillations. Based on the bimodal ISO index of MJO mode, 22 successive and 5 primary events with strong magnitude and clear propagation are identified in November-April, 1982-2011. The evolution of successive MJO events are analyzed through the diagnosis of low-tropospheric moisture and column-integrated MSE budget. To discuss the role of different processes (e.g., moisture advection, radiation, and surface turbulent fluxes) in different stages, the life cycle of MJO are further divided into four stages (i.e., suppressed, cloud developing, convective, and decaying) based on the evolution of OLR anomaly and low-level moistures.

The results of low-level moisture budget show that while vertical advection and $-Q_2$



are the large terms, the evolution of tendency resembles the horizontal advection, with meridional advection contributing to the eastward propagation over MC/WP and zonal advection contributing to the growing over IO. A scale-separated budget is calculate to investigate the influence of scale interaction on intraseasonal variability. The result shows that the leading term in the moisture advection, both horizontal and vertical, is the advection of mean moisture by the MJO flow. A column-integrated MSE budget is further performed to provide insight into the role of diabatic processes in the evolution of MJO. It suggests that the MSE anomalies associated with the MJO are mainly maintained by radiative feedback, with surface turbulent flux feedback playing a secondary role. The slight phase lag of longwave heating and surface latent heat flux with column-integrated MSE also acts to slows down the eastward propagation. Overall, the moisture and MSE evolution over MC is consistent with IO except that meridional advection is more essential and the synoptic disturbances also contribute to the eastward propagation.

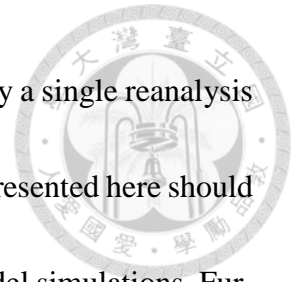
The composite of MJO successive events indicates that the suppressed convection of previous events plays an important role in the initiation and propagation of subsequent events. The low-level easterlies and poleward flows induced by the dry anomaly of previous events advect moisture from the warm pool and equator to the Indian Ocean and off-equatorial region over Maritime Continent. These moistening destabilize the atmos-



phere and provide a favorable environment for the potential development of MJO convection. In addition, as the large-scale downward motion associated with the suppressed convection confines the development of convection, the cloud population is dominated by non-precipitating shallow convection. The negative $-Q_2$ in the suppressed stage suggests the collective effect of moistening by re-evaporation of shallow convection. The enhanced radiative cooling due to the lack of deep convection also acts to destabilize the atmosphere.

Broadly, our conclusions are consistent with previous research using field observation during DYNAMO/CINDY IOP period, reanalysis, and model simulation (e.g., Sobel et al. 2014; Tseng et al. 2015; Kim et al. 2014; Zhao et al. 2013; Hsu and Li 2012; Wolding and Maloney 2015; Chikira 2014). The main progress of this study is that we use an objective method to separate the individual attribution from current and previous events. The relative contributions of large-scale wave dynamics and local physical processes to the initiation and propagation are investigated under different sets of MJO events, i.e., successive and primary. The systematic comparison between Indian Ocean and maritime Continent is another contribution. In the current study, we only analyze the successive MJO events and discuss the influence by previous events. To identify the genuine initiation mechanisms that are not associated with previous MJO, the next step is applying the same diagnosis method to the primary events. The BSISO events dominating the boreal

summer will be also investigated in future study. Moreover, since only a single reanalysis product was implemented in this study, the robustness of the results presented here should be tested by using other reanalysis, independent observation, and model simulations. Further investigation into the role of shallow convection during suppressed stage by using field observation is also needed.





References

- Adames, A. F., and D. Kim, 2016: The MJO as a dispersive, convectively coupled moisture wave: Theory and observations. *J. Atmos. Sci.*, **73**, 913–941
- Andersen, J. A., and Z. Kuang, 2012: Moist static energy budget of MJO-like disturbances in the atmosphere of a zonally symmetric aquaplanet. *J. Climate*, **25**, 2782–2804.
- Benedict, J. J., and D. A. Randall, 2007: Observed characteristics of the MJO relative to maximum rainfall. *J. Climate*, **64**, 2332–2354.
- Bladé, I., and D. L. Hartmann, 1993: Tropical intraseasonal oscillations in a simple nonlinear model. *J. Atmos. Sci.*, **50**, 2922–2939.
- Chang, C.-P., 1977: Viscous internal gravity waves and low-frequency oscillations in the tropics. *J. Atmos. Sci.*, **34**, 901–912.
- Chikira, M., 2014: Eastward-propagating intraseasonal oscillation represented by Chikira–Sugiyama cumulus parameterization. Part II: Understanding moisture variation under weak temperature gradient balance. *J. Atmos. Sci.*, **71**, 615–639.
- Hannah, W. M., and E. D. Maloney, 2011: The role of moisture–convection feedbacks in simulating the Madden–Julian oscillation. *J. Climate*, **24**, 2754–2770.
- Hsu, P.-C., and T. Li, 2012: Role of the boundary layer moisture asymmetry in causing the eastward propagation of the Madden–Julian oscillation. *J. Climate*, **25**, 4914–4931.



Hu, Q., and D. A. Randall, 1994: Low-frequency oscillations in radiative–convective systems. *J. Atmos. Sci.*, **51**, 1089–1099.

Johnson, R. H., P. E. Ciesielski, J. H. Ruppert, and M. Katsumata, 2015: Sounding-based thermodynamic budgets for DYNAMO. *J. Atmos. Sci.*, **72**, 598–622

Kemball-Cook, S. R., and B. C. Weare, 2001: The onset of convection in the Madden–Julian oscillation. *J. Climate*, **14**, 780–793.

Kerns, B. W., and S. Chen, 2014: Equatorial dry air intrusion and related synoptic variability in MJO initiation during DYNAMO. *Mon. Wea. Rev.*, **142**, 1326–1343.

Kikuchi, K., B. Wang, Y. Kajikawa, 2012: Bimodal representation of the tropical intraseasonal oscillation. *Clim. Dyn.*, **38**, 1989–2000.

Kiladis, G. N., K. H. Straub, and P. T. Haertel, 2005: Zonal and vertical structure of the Madden–Julian oscillation. *J. Atmos. Sci.*, **62**, 2790–2809.

Kim, D., J.-S. Kug, and A. H. Sobel, 2014: Propagating versus nonpropagating Madden–Julian oscillation events. *J. Climate*, **27**, 111–125.

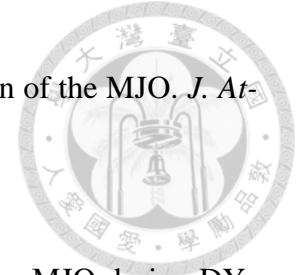
Kim, H.-M., P. J. Webster, V. E. Toma, and D. Kim, 2014: Predictability and prediction skill of the MJO in two operational forecasting systems. *J. Climate*, **27**, 5364–5378.

Lau, K.-M., and L. Peng, 1987: Origin of low-frequency (intraseasonal) oscillations in the tropical atmosphere. Part I: Basic theory. *J. Atmos. Sci.*, **44**, 950–972.

Lee, J.-Y., B. Wang, M. Wheeler, X. Fu, D. Waliser, and I.-S. Kang, 2013: Real-time



- multivariate indices for the boreal summer intraseasonal oscillation over the Asian summer monsoon region. *Clim. Dyn.*, **40**, 493–509.
- Liebmann, B., and C. A. Smith, 1996: Description of a complete (interpolated) outgoing longwave radiation dataset. *Bull. Amer. Meteor. Soc.*, **77**, 1275–1277.
- Madden, R. A., and P. R. Julian, 1972: Description of global-scale circulation cells in the tropics with a 40–50 day period. *J. Climate*, **29**, 2665–2690.
- Maloney, E. D., and B. Wolding (2015), Initiation of an intraseasonal oscillation in an aquaplanet general circulation model, *J. Adv. Model. Earth Syst.*, **7**, 1956–1976.
- Matthews, A., 2008: Primary and successive events in the Madden–Julian Oscillation. *Q. J. R. Meteorol. Soc.* **134**, 439–453.
- Neena, J., J. Y. Lee, D. Waliser, B. Wang, and X. Jiang, 2014: Predictability of the Madden–Julian oscillation in the Intraseasonal Variability Hindcast Experiment (ISVHE). *J. Climate*, **27**, 4531–4543.
- Peatman, S. C., A. J. Matthews, and D. P. Stevens, 2014: Propagation of the Madden–Julian oscillation through the Maritime Continent and scale interaction with the diurnal cycle of precipitation. *Quart. J. Roy. Meteor. Soc.*, **140**, 814–825.
- Sobel, A., and E. Maloney, 2012: An idealized semi-empirical framework for modeling the Madden–Julian oscillation. *J. Atmos. Sci.*, **69**, 1691–1705.



——, and ——, 2013: Moisture modes and the eastward propagation of the MJO. *J. Atmos. Sci.*, **70**, 187–192.

——, S. Wang, and D. Kim, 2014: Moist static energy budget of the MJO during DYNAMO. *J. Atmos. Sci.*, **71**, 4276–4291.

Stephens, G. L., P. J. Webster, R. H. Johnson, R. Engelen, and T. S. L’Ecuyer, 2004: Observational evidence for the mutual regulation of the tropical hydrological cycle and tropical sea surface temperatures. *J. Climate*, **17**, 2213–2224.

Tseng, K.-C., C.-H. Sui, and T. Li, 2015: Moistening Processes for Madden-Julian Oscillations during DYNAMO/CINDY. *J. Climate*, **28**, 3041–3058.

Wang, B., 2011: Theory. In *Intraseasonal Variability in the Atmosphere-Ocean Climate System*, Springer, 307–360.

——, and G. Chen, 2016: A unified theory for essential dynamics of Madden-Julian Oscillation. *Clim. Dyn.*, submitted

——, and T. Li, 1994: Convective interaction with boundary dynamics in the development of a tropical intraseasonal system. *J. Atmos. Sci.*, **51**, 1386–1400.

Wheeler, M., and G. N. Kiladis, 1999: Convectively coupled equatorial waves: Analysis of clouds and temperature in the wavenumber–frequency domain. *J. Atmos. Sci.*, **56**, 374–399.

——, ——, and P. J. Webster, 2000: Large-scale dynamical fields associated with convectively coupled equatorial waves. *J. Atmos. Sci.*, **57**, 613–640.



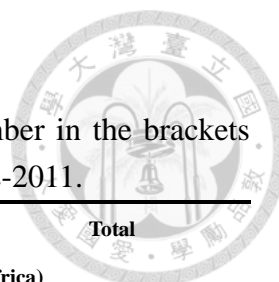
——, and H. H. Hendon, 2004: An all-season real-time multivariate MJO index: Development of an index for monitoring and prediction. *Mon. Wea. Rev.*, **132**, 1917–1932.

Wolding, B. O., and E. D. Maloney, 2015: Objective diagnostics and the Madden–Julian oscillation. Part I: Methodology. *J. Climate*, **28**, 4127–4140.

Wu, C.-H., and H.-H. Hsu, 2009: Topographic influence on the MJO in the Maritime Continent. *J. Climate*, **22**, 5433–5448.

Yanai, M., S. Esbensen, and J.-H. Chu, 1973: Determination of bulk properties of tropical cluster from large-scale heat and moisture budget. *J. Atmos. Sci.*, **30**, 611–627.

Zhao, C., T. Li, and T. Zhou, 2013: Precursor signals and processes associated with MJO initiation over the tropical Indian Ocean. *J. Climate*, **26**, 291–307.



Tables

Table 1. Number of days for each of the four categories. The number in the brackets shows the ratio to the total number of days (10957 days) during 1982-2011.

	A (Indian Ocean)	B (Maritime Continent)	C (Western Pacific)	D (West Hem. & Africa)	Total
MJO	1001 (9.14%)	807 (7.27%)	978 (8.93%)	932 (8.51%)	2232 (33.93%)
BSISO	1231 (11.23%)	972 (8.87%)	1245 (11.36%)	985 (8.99%)	4433 (40.46%)
Total	2232 (20.37%)	1779 (16.24%)	2223 (20.29%)	1917 (17.50%)	8151 (74.39%)

Table 2. Number of instances of the successive and primary events for ISO (left). Number of consecutive events for ISO (right). Single means there is no consecutive event (DABCD), double indicates a continuation of two events (DABCDABCD), and so forth.

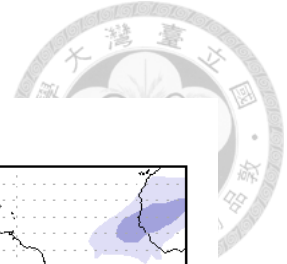
	Successive (DABCD)	Primary (NABCD)	Quadruple	Triple	Double	Single	Total
MJO	22	5	1	2	1 (1 BSISO)	16	27
BSISO	23	8	0	0	3	24	31
Total	45	13	1	2	4	40	58

Table 3. The low-level moisture budget of four stages over the Central Indian Ocean. 95% statistically significant budget terms are shown in boldface.

CIO	Tendency	Zonal Advection	Meridional Advection	Vertical Advection	-Q ₂
Suppressed	2.88	3.11	-1.00	-5.80	0.58
Cloud Developing	3.83	3.72	-0.88	27.13	-26.14
Convective	-5.61	-4.54	0.25	20.42	-21.73
Decaying	-8.61	-8.21	0.76	-7.50	6.35

Table 4. As in Table 3, expect for Maritime Continent.

MC	Tendency	Zonal Advection	Meridional Advection	Vertical Advection	-Q ₂
Suppressed	2.21	1.70	1.63	-9.67	8.54
Cloud Developing	1.95	2.43	1.71	17.91	-20.10
Convective	-2.69	-1.18	-0.89	21.05	-21.67
Decaying	-5.20	-5.26	-2.87	5.64	-2.71



Figures

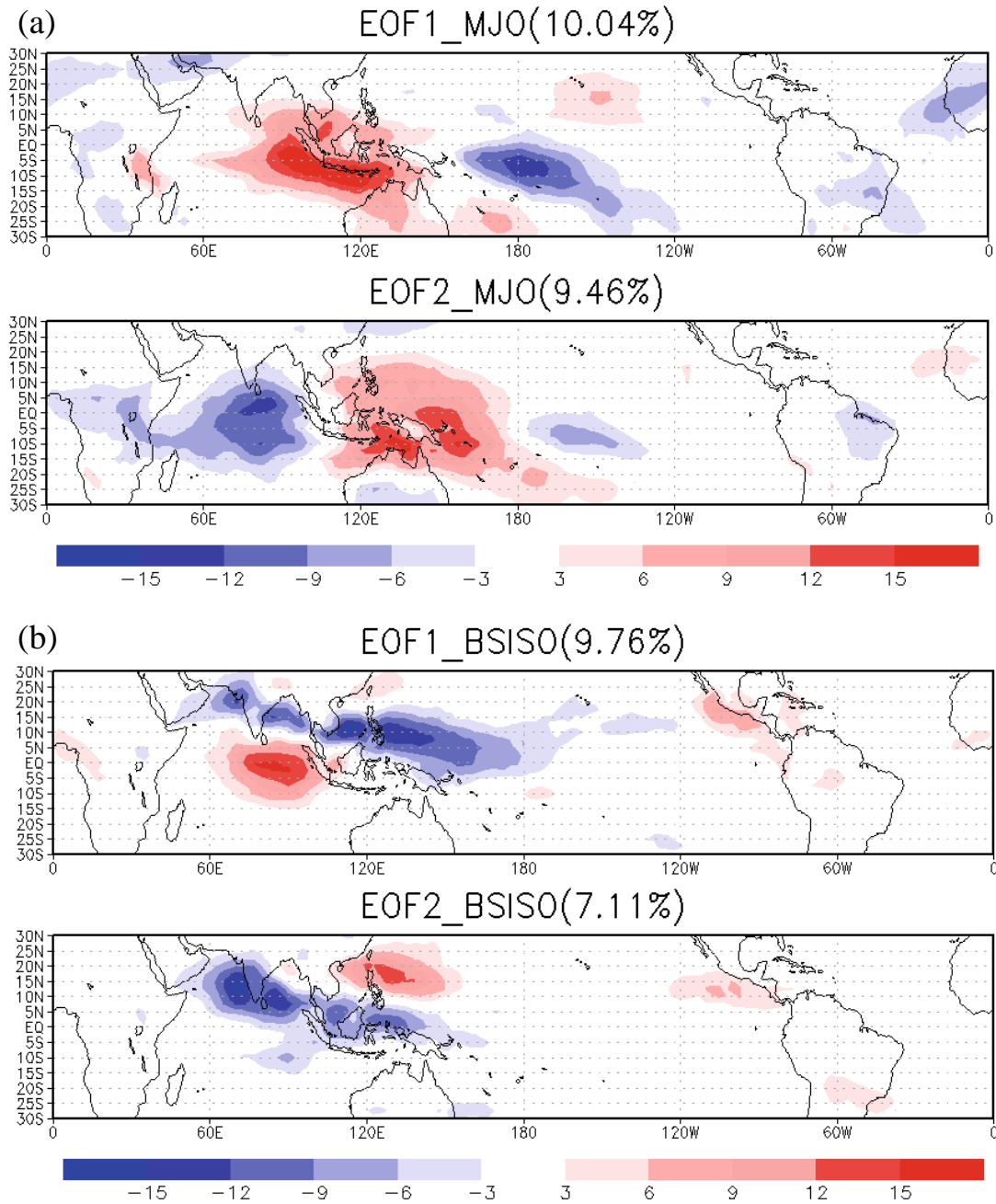


FIG. 1. The EOF patterns of the 25-90 day filtered OLR during (a) boreal winter (DJF) and (b) boreal summer (JJA). The number in the brackets shows the contribution of each EOF mode to total variance. The OLR values are multiplied by one standard deviation of the corresponding principal components to obtain the typical value and unit ($W m^{-2}$) for intraseasonal oscillations.

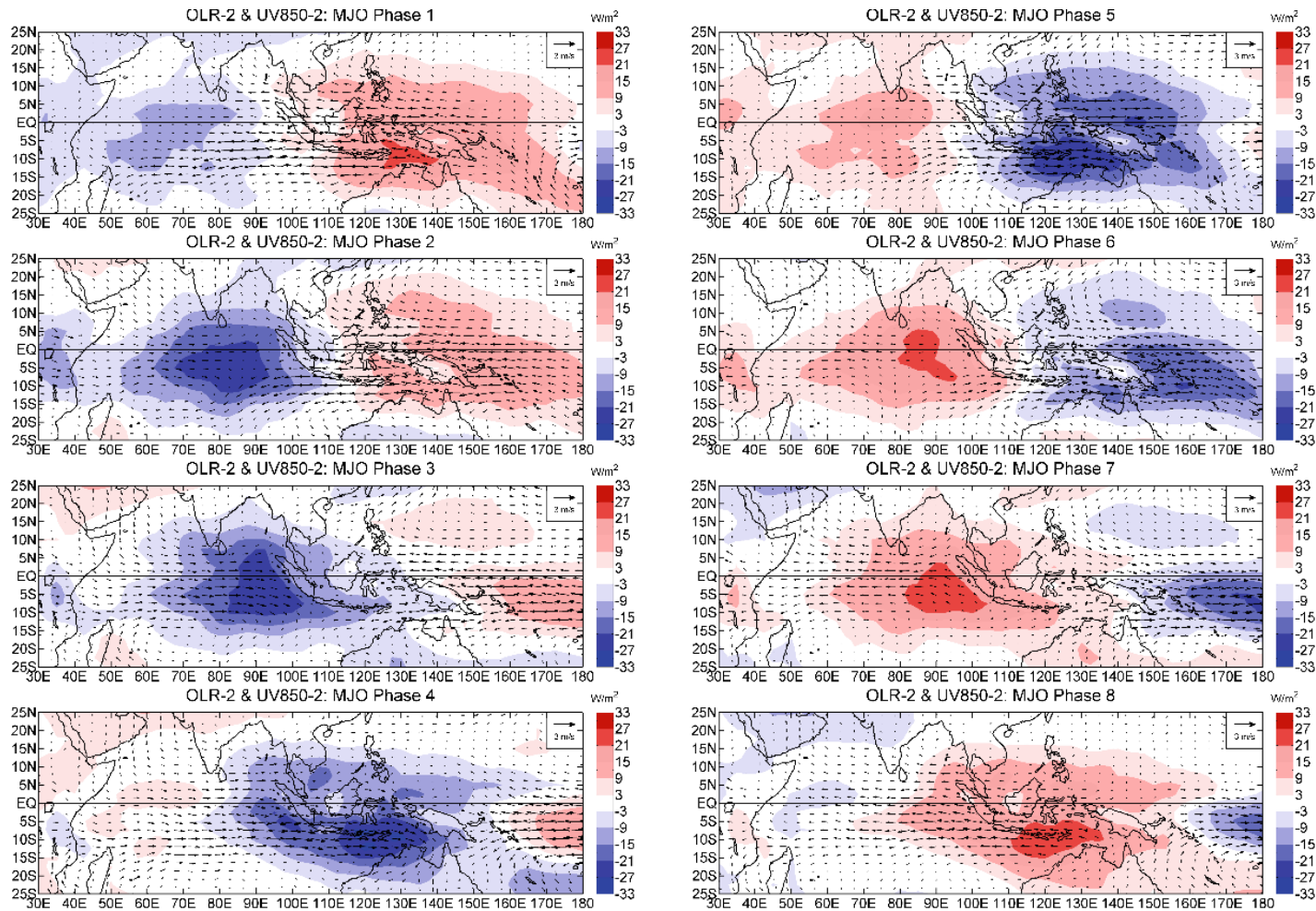


FIG. 2. The composite life cycle of the MJO mode. The 20-60 day filtered OLR (shading, $W m^{-2}$) and horizontal wind fields at 850 hPa (vector, $m s^{-1}$).

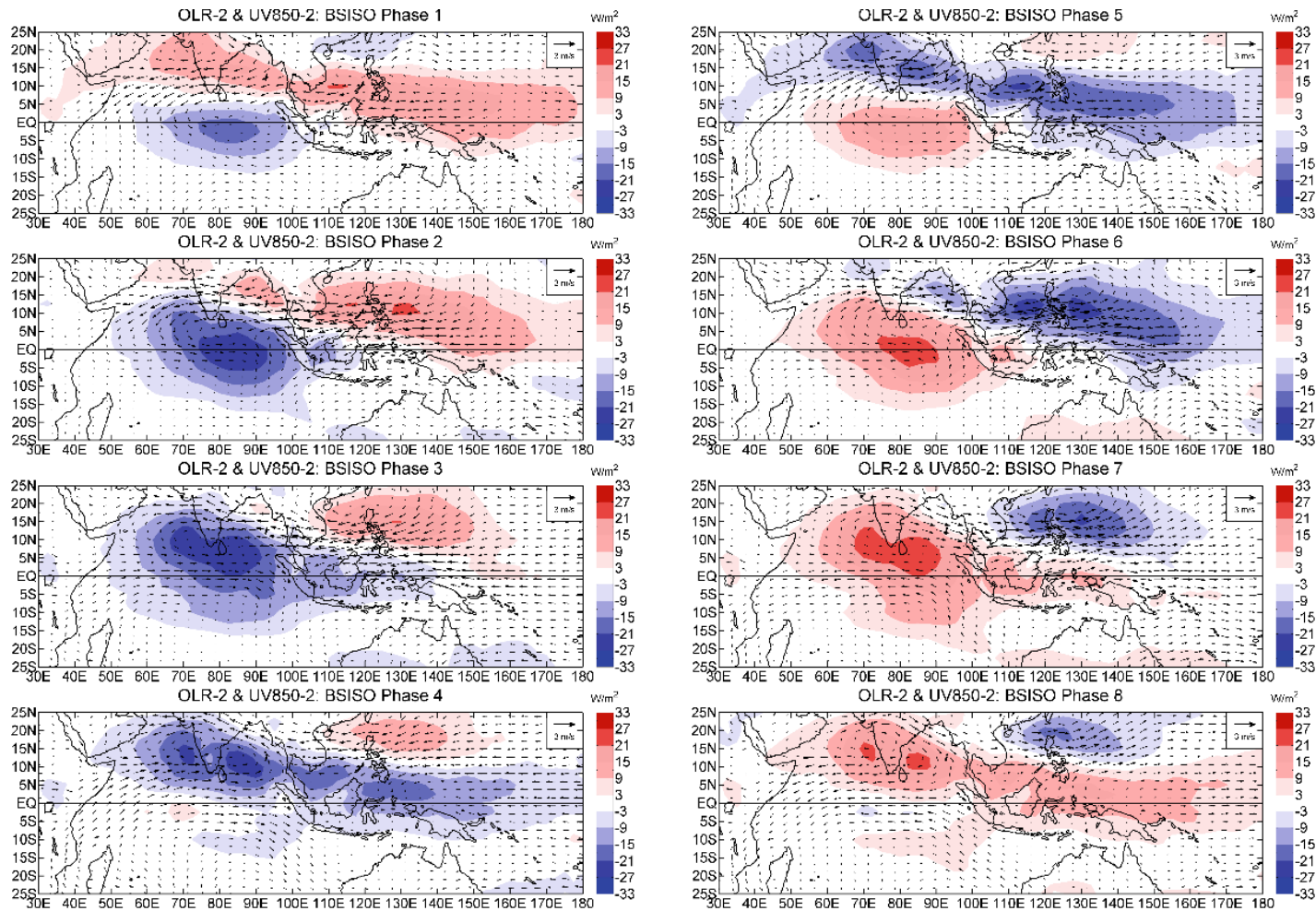


FIG. 3. As in Fig. 2, except for the BSISO mode.

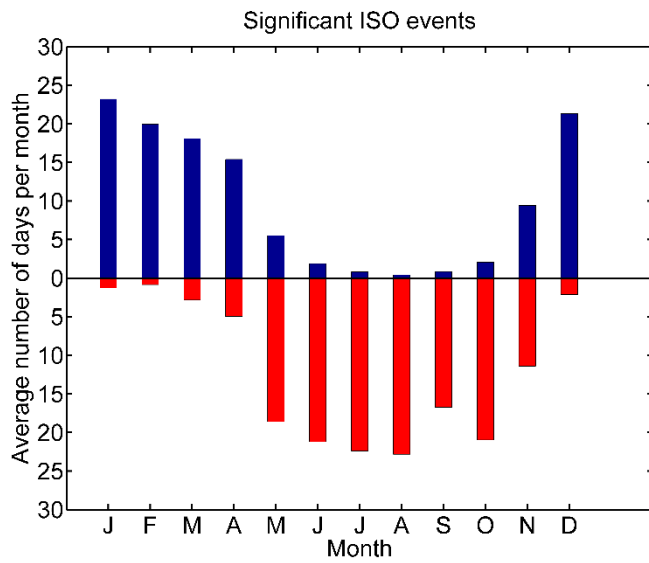


FIG. 4. Average number of days during which significant ISO (amplitude ≥ 1) is present in a month. The days are normalized such that they are the ratio of the number of days classified as the significant MJO mode (upper, blue) or significant BSISO mode (lower, red) to the number of days during 1982–2011 times the number of days in the month of common year.

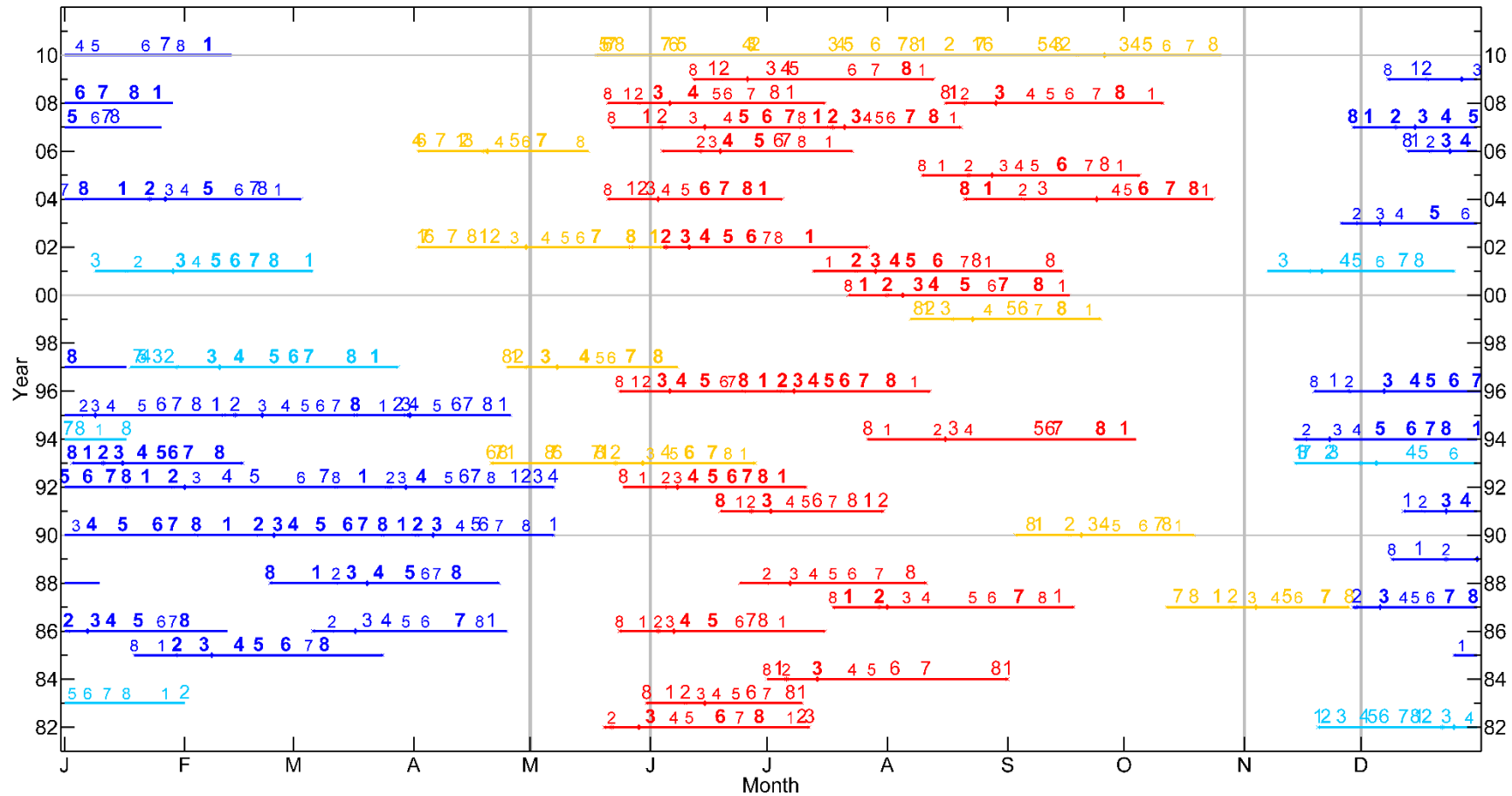


FIG. 5. The duration and corresponding bimodal phases for each selected MJO (blue) and BSISO (red) event in 1982-2011. The successive (primary) events are presented in dark (light) color. The width of the line and the font size of phase number denote the strength of the events. The gray vertical lines mark the transitional months, i.e., May and November.

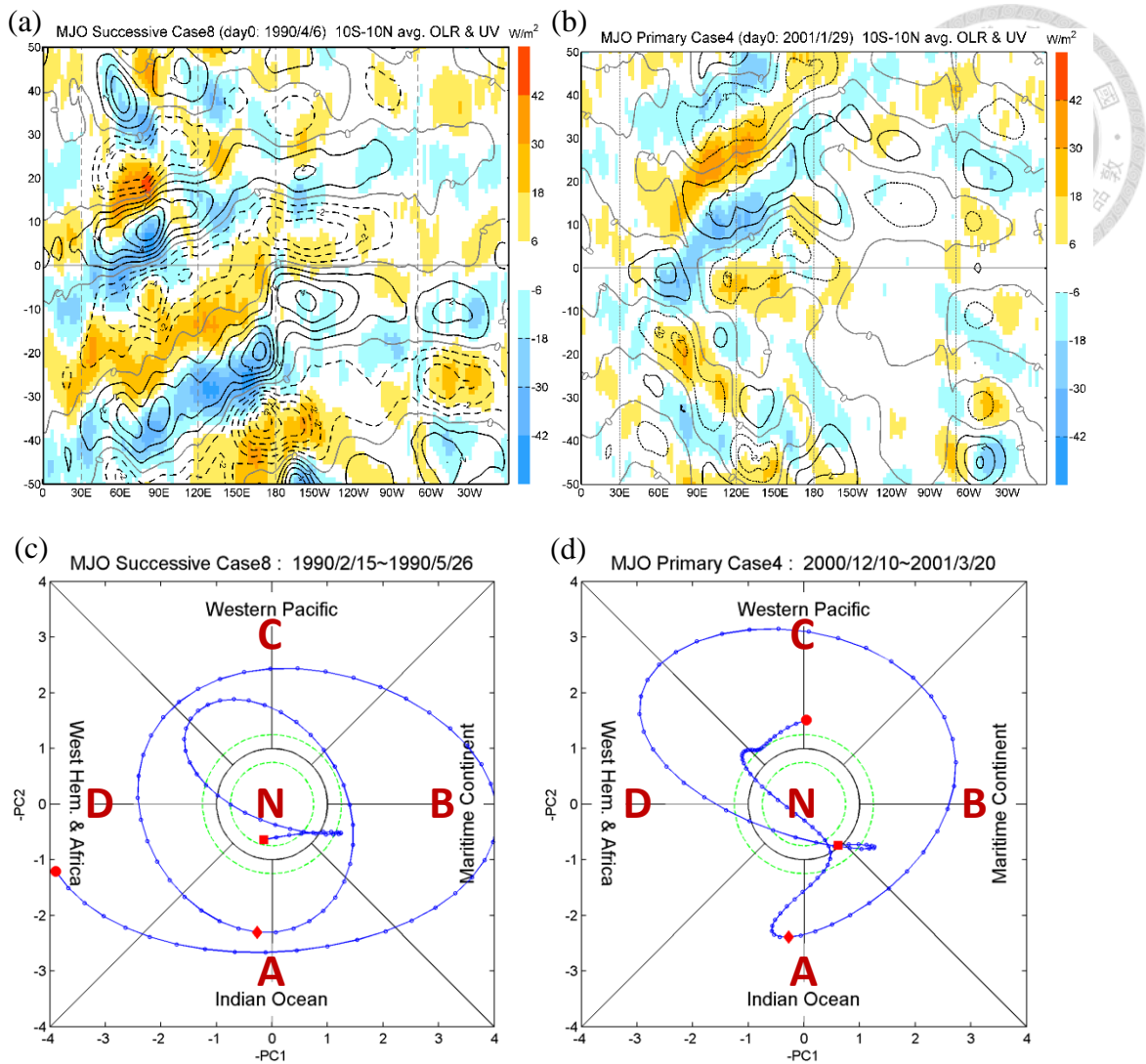


FIG. 6. (a) Hovmöller diagram of 10°S - 10°N averaged, 20-60 day filtered OLR (shading, W m^{-2}) and low-level zonal winds (contours, interval of 1 m s^{-1}) for a successive event with a 101-day period (day 0 ± 50 days) from 15 February 1990 to 26 May 1990. Day 0 is defined as the day when OLR over Indian Ocean reaches minimum. (c) The corresponding phase diagram. The first ($t = -50$), central ($t = 0$), and last ($t = 50$) days are denoted by a filled circle, a filled diamond, and a filled square, respectively. (b) and (d) are as (a) and (c), expect for a primary event with a 101-day period from 10 December 2000 to 20 March 2001. The text N denotes the region where the amplitude is smaller than 1. See text for details.

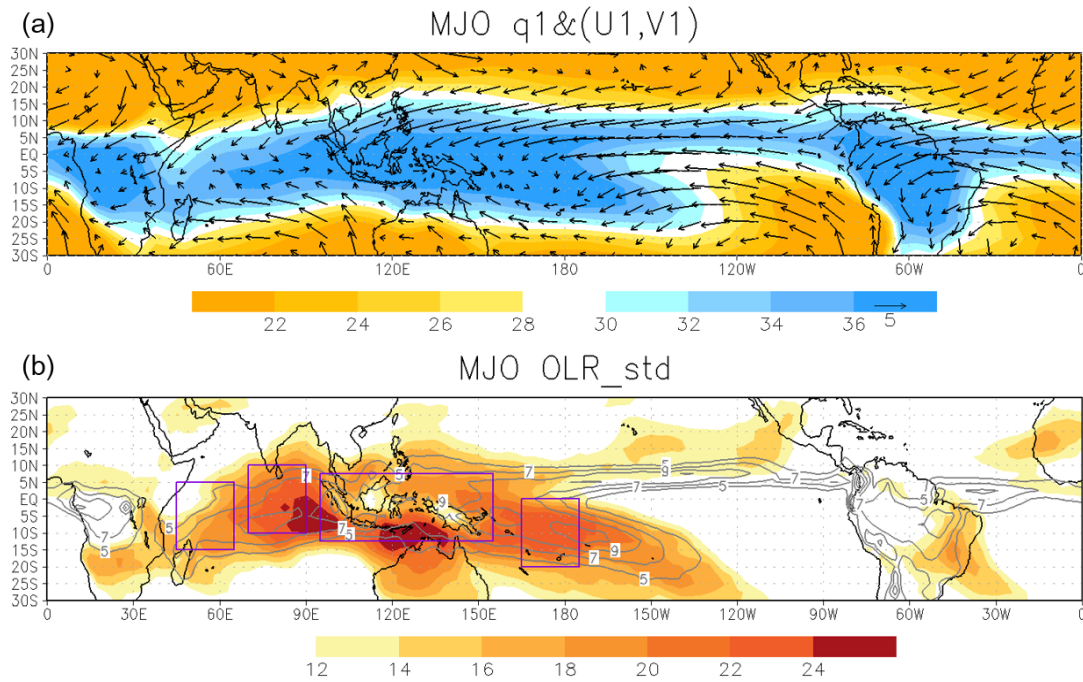


FIG. 7. (a) 1000-700 hPa integrated low-frequency moisture (shading, g kg⁻¹) and wind fields (vector, m s⁻¹) and (b) standard deviation of 20-60 day filtered OLR (shading, W m⁻²) and seasonal mean precipitation (contours, mm day⁻¹) during boreal winter. The purple boxes marks the locations of four MJO activity centers in sequence from the left side to the right: WIO (15°S-5°N, 45°E-65°E), CIO (10°S-10°N, 70°E-90°E), MC (12.5°S-7.5°N, 100°E-155°E), and WP (12.5°S-7.5°N, 100°E-155°E).

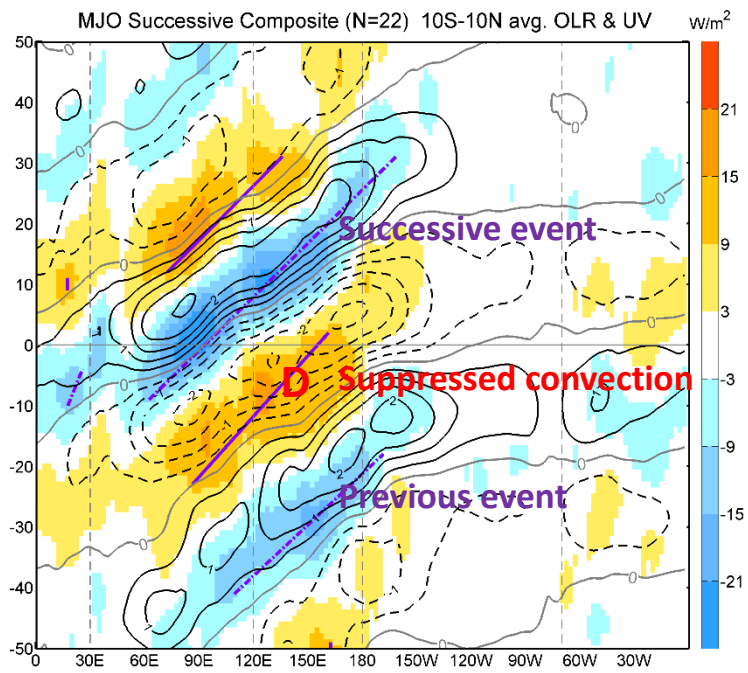


FIG. 8. Composites Hovmöller diagram of 10°S-10°N averaged, 20-60 day filtered OLR (shading, $W m^{-2}$) and low-level zonal winds (contours, interval of $1 m s^{-1}$). The purple solid (dashed) lines mark the location of OLR maximum (minimum). The red D indicates the positive OLR anomaly associated with previous events.

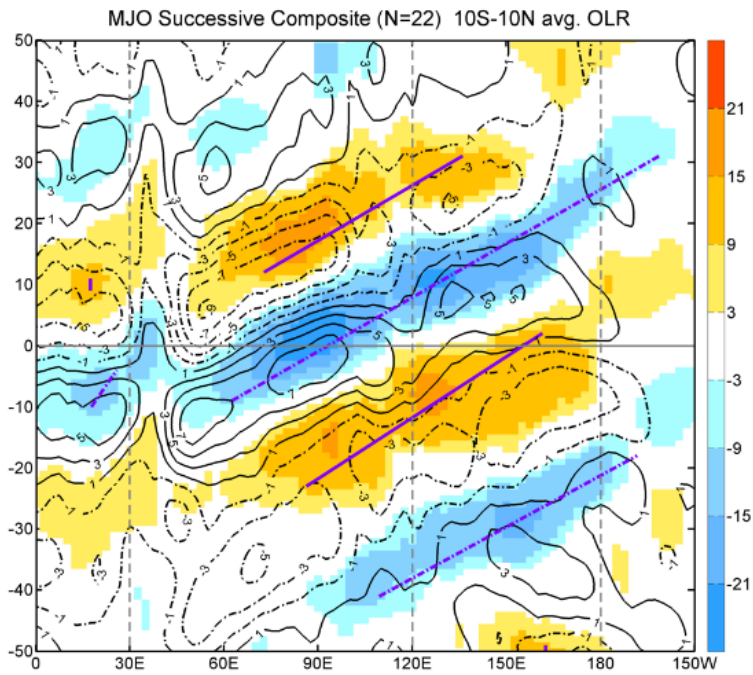


FIG. 9. Composites Hovmöller diagram of 10°S-10°N averaged, 20-60 day filtered OLR (shading, W m^{-2}) and low-tropospheric moisture (contours, interval of 10^6 J m^{-2} ; L is absorbed into q). The purple solid (dashed) lines mark the location of OLR maximum (minimum).

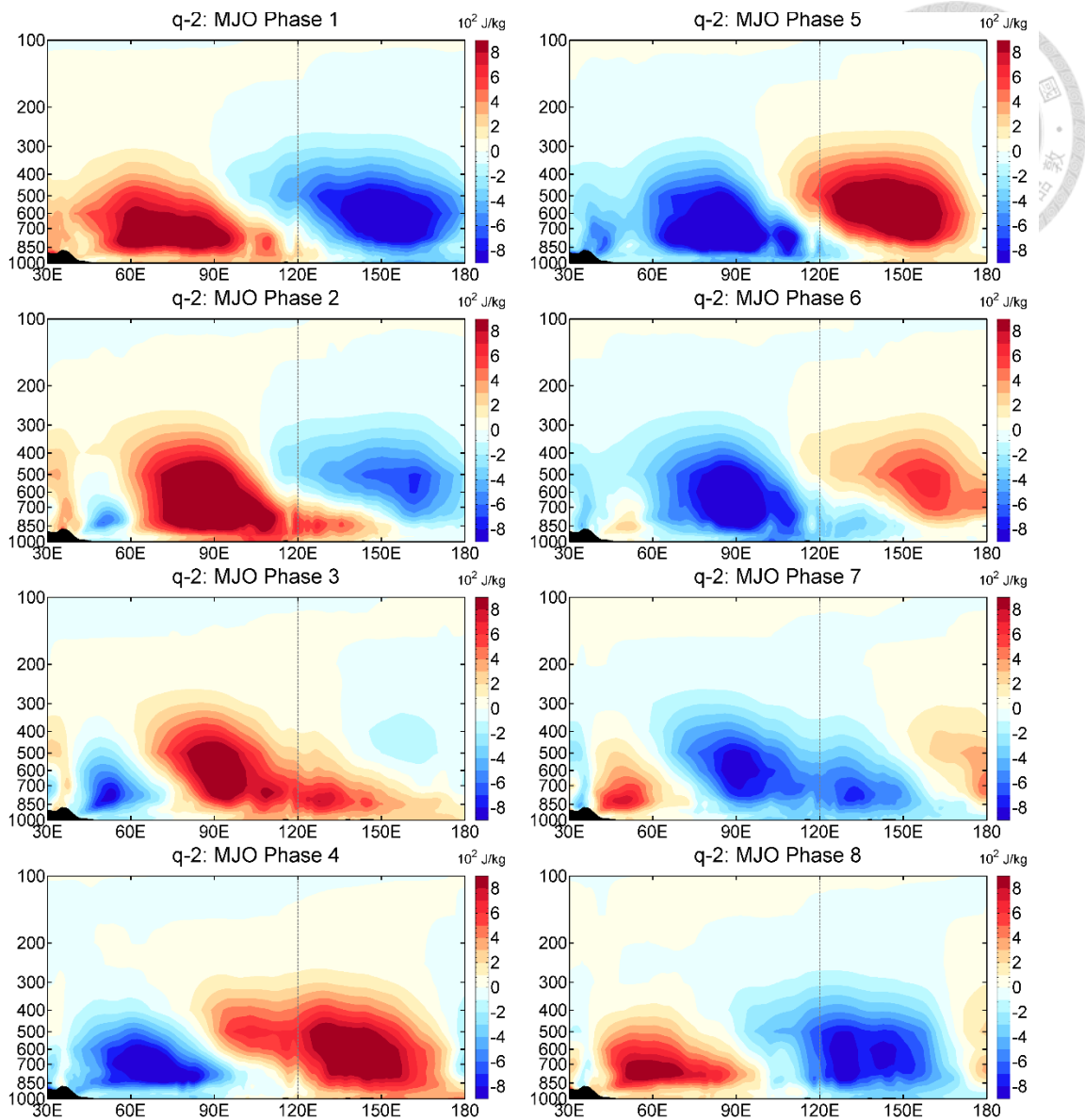


FIG. 10. Composites zonal-vertical distribution of 10°S - 10°N averaged, 20-60 day filtered moisture (shading, interval of 10^2 J kg^{-1} ; L is absorbed into q) in eight MJO bimodal index phases.

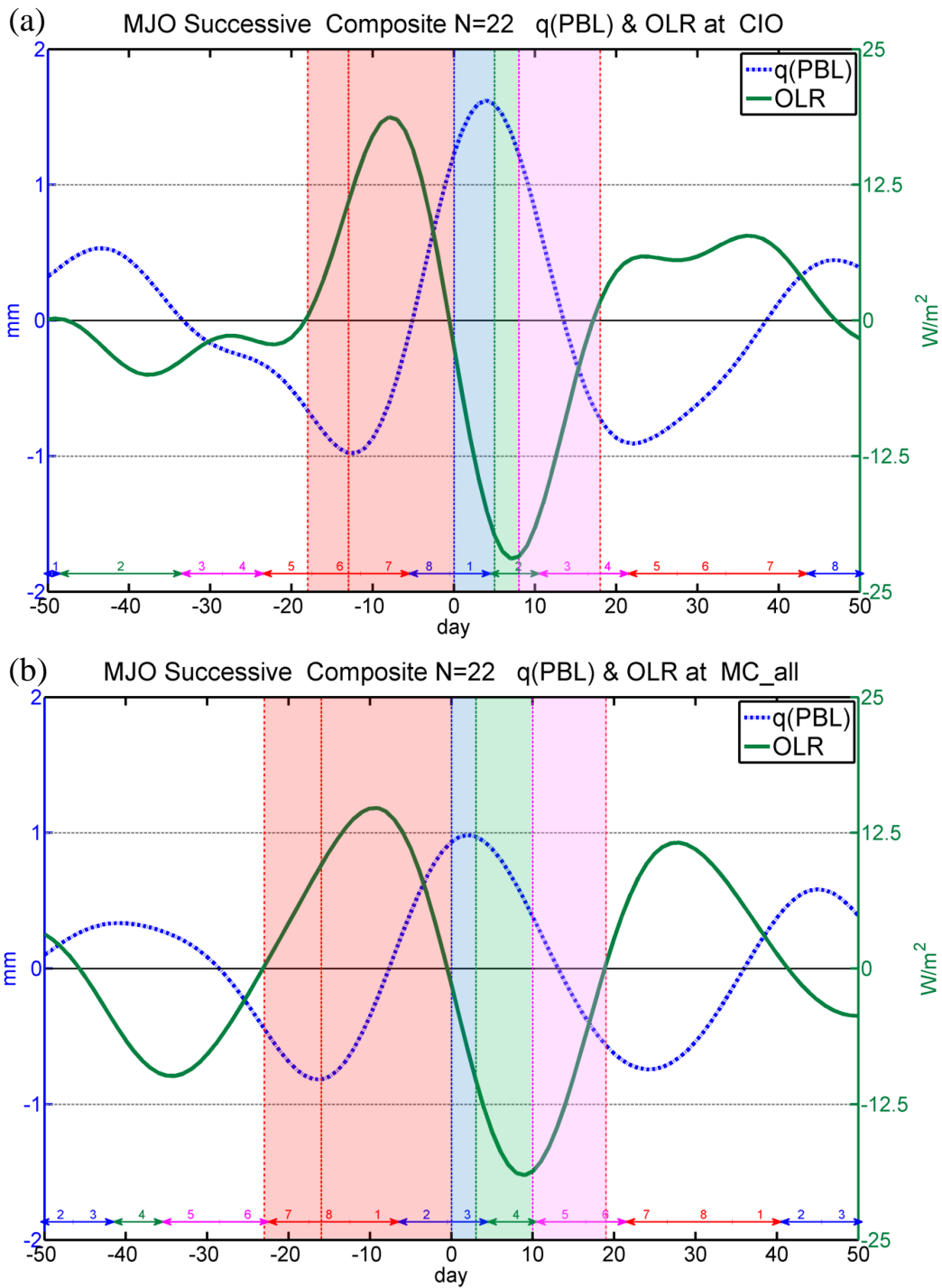


FIG. 11. (a) Time series of 20-60 day OLR anomaly (green solid line) and low-tropospheric moistures (blue dashed line) over Central Indian Ocean. Suppressed (red), cloud developing (blue), convective (green), and decaying (pink) stages are shaded. The day 0 in this figure represent the day when the OLR anomaly turns negative. The numbers above the x axis are the corresponding MJO bimodal index phase. (b) is as (a), expect for Maritime Continent.

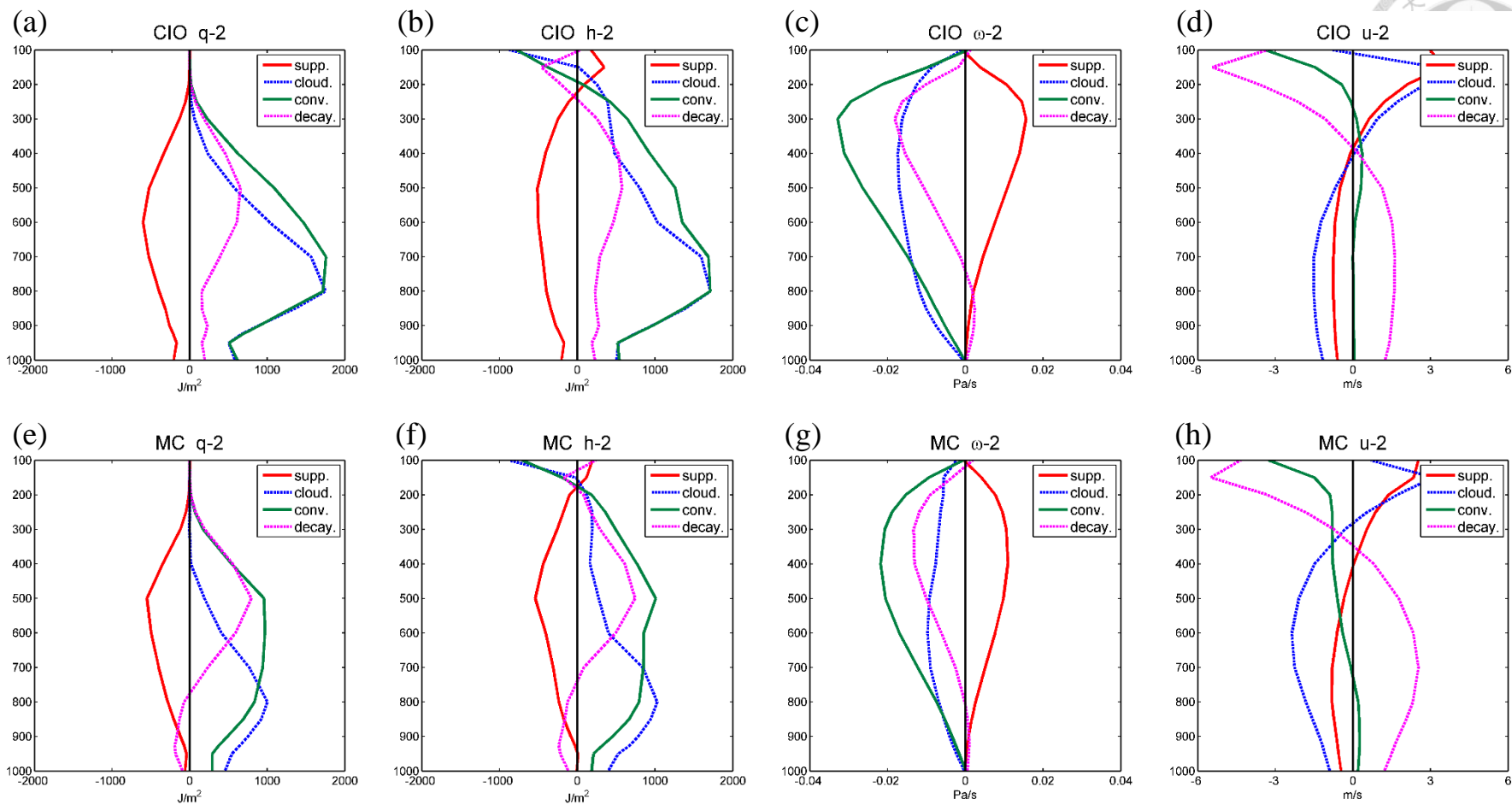
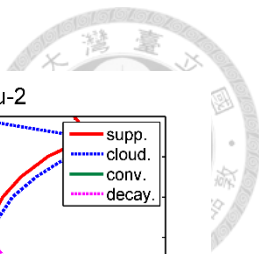


FIG. 12. Vertical structure of 20-60 day filtered (a) moisture, (b) MSE, (c) pressure velocity, and (d) zonal winds over Central Indian Ocean in four stages (suppressed in red, cloud developing in blue dashed, convective in green, and decaying in pink dashed). (e)-(h) are as (a)-(d), expect for Maritime Continent.

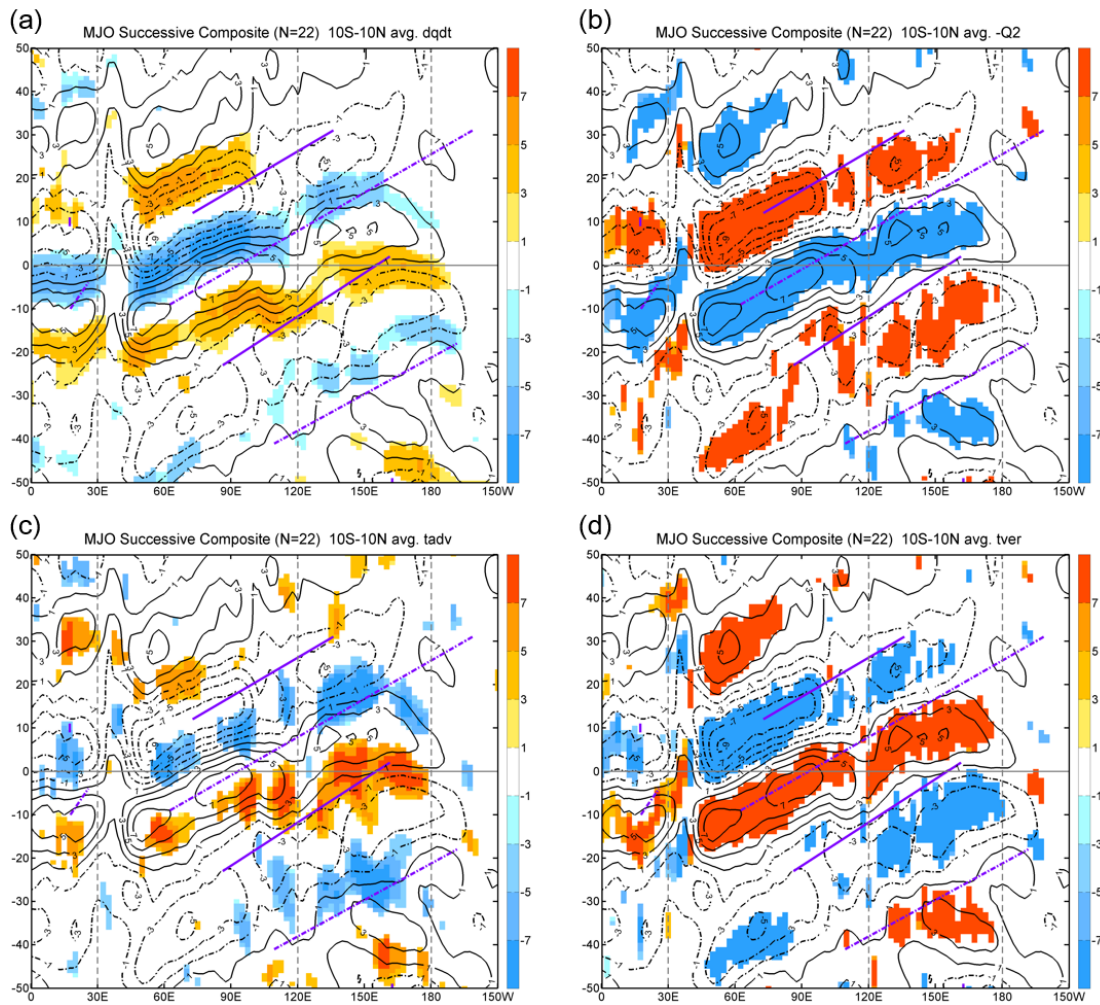


FIG. 13. Composit ed Hovmöller diagram of $10^{\circ}S-10^{\circ}N$ averaged, 20-60 day filtered low-tropospheric moisture budget terms (shading, $W m^{-2}$): (a) tendency, (b) $-Q_2$, (c) horizontal advection, and (d) vertical advection. Budget terms are shown only when they are statistically significant at 95% confidence level. Contoured in each panel is low-tropospheric moisture ($J m^{-2}$) anomaly with interval of $10^6 J m^{-2}$. The purple solid (dashed) lines mark the location of OLR maximum (minimum).

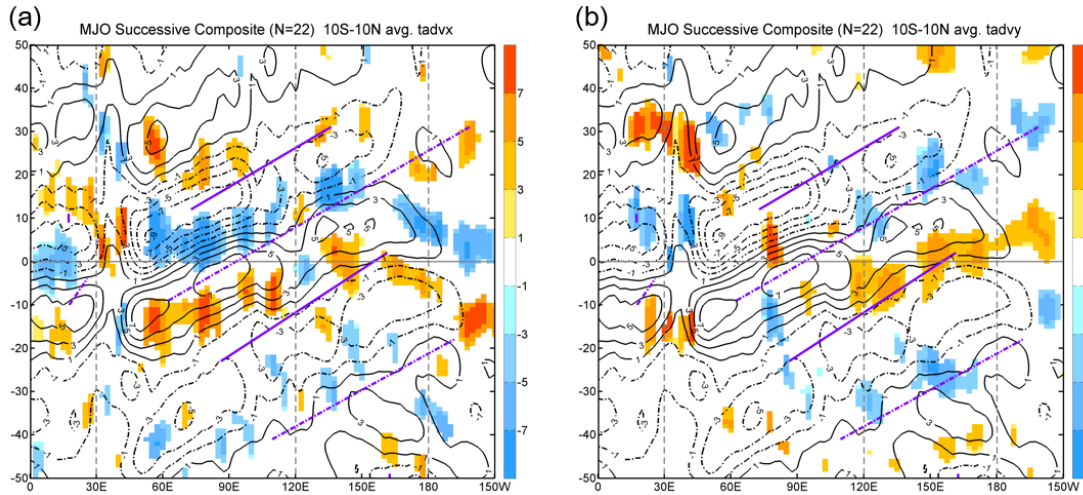


FIG. 14. As in Fig. 13, expect for (a) zonal advection and (b) meridional advection term. Contoured in each panel is low-tropospheric moisture (J m^{-2}) anomaly with interval of 10^6 J m^{-2} . The purple solid (dashed) lines mark the location of OLR maximum (minimum).

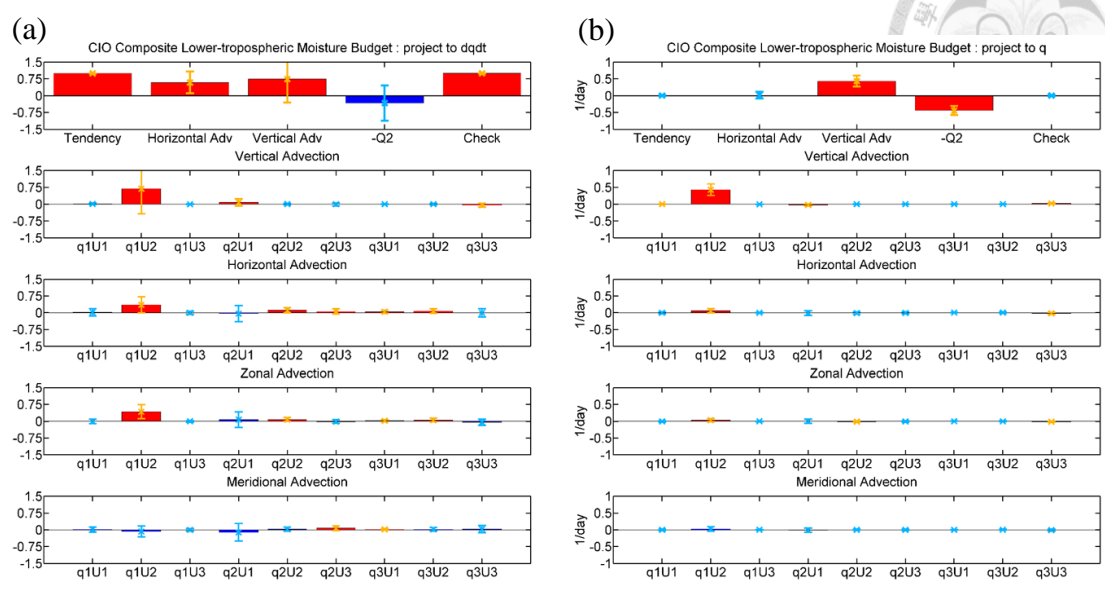
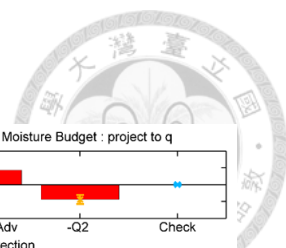


FIG. 15. (a) The projection of scale-separated budget terms to local moisture tendency over Central Indian Ocean. All terms are normalized by the projection of moisture tendency itself (all variables are non-dimensional). 95% statistically significant budget terms are shown in red. The error bar presents the standard deviation of each term. (b) is as (a), except for the projection of scale-separated budget terms to moisture anomaly $[q]'$. All terms are normalized by the projection of moisture anomaly itself (all variables are shown in growth rate; day^{-1}).

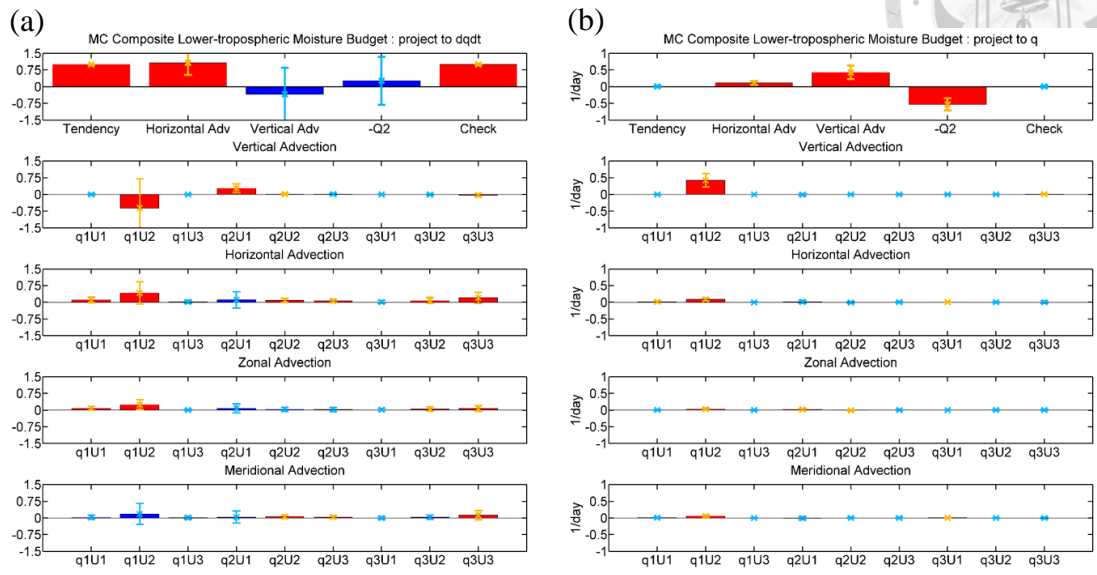
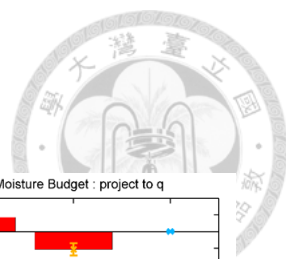


FIG. 16. As in Fig. 15, expect for Maritime Continent.

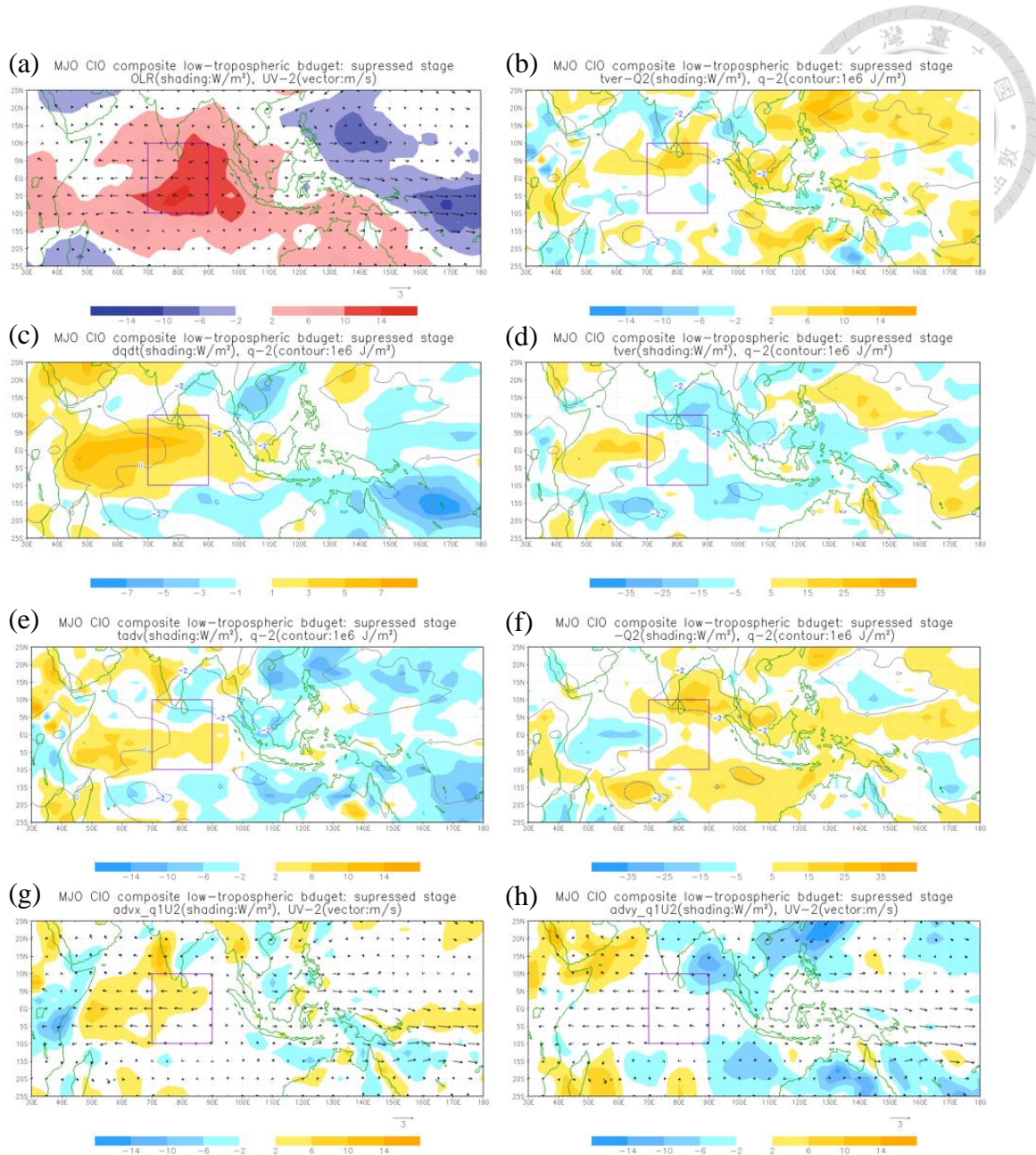


FIG. 17. (a) 20-60 day filtered OLR (shading, W m^{-2}) and low-level winds (vector, m s^{-1}); Horizontal distribution of low-tropospheric moisture budget terms (shading, W m^{-2}) during the CIO suppressed stage: (b) $[\omega \partial q / \partial p]' - Q_2$, (c) tendency, (d) vertical advection, (e) horizontal advection, (f) $-Q_2$. Contoured in each panel is the low-tropospheric moisture (J m^{-2}) anomaly with interval of 10^6 J m^{-2} . (g) $-[u_2 \partial q_1 / \partial x]'$, (h) $-[v_2 \partial q_1 / \partial y]'$ and 20-60 day filtered low-level winds (vector, m s^{-1}).

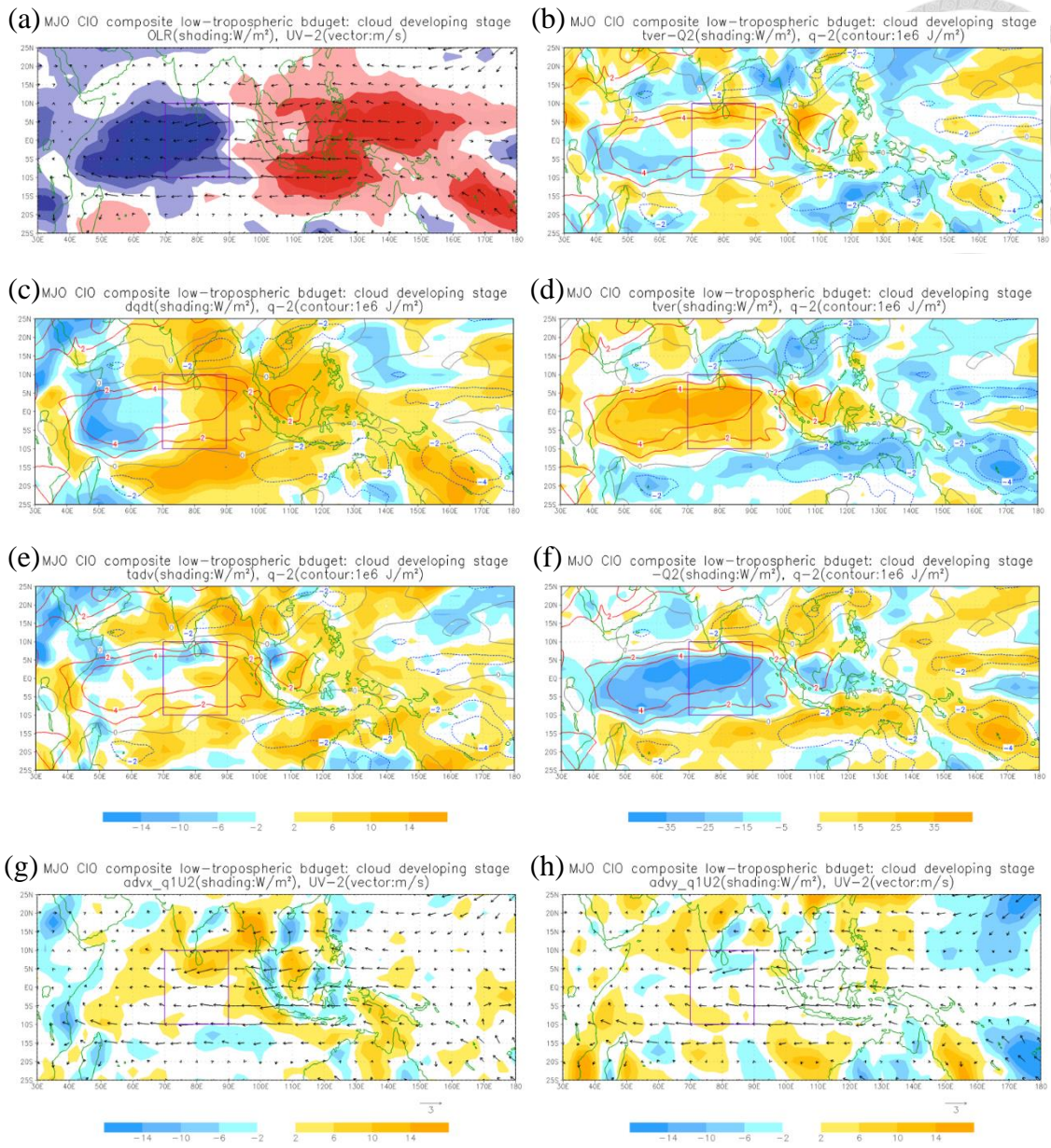


FIG. 18. As in Fig. 17, except for CIO cloud developing stage.

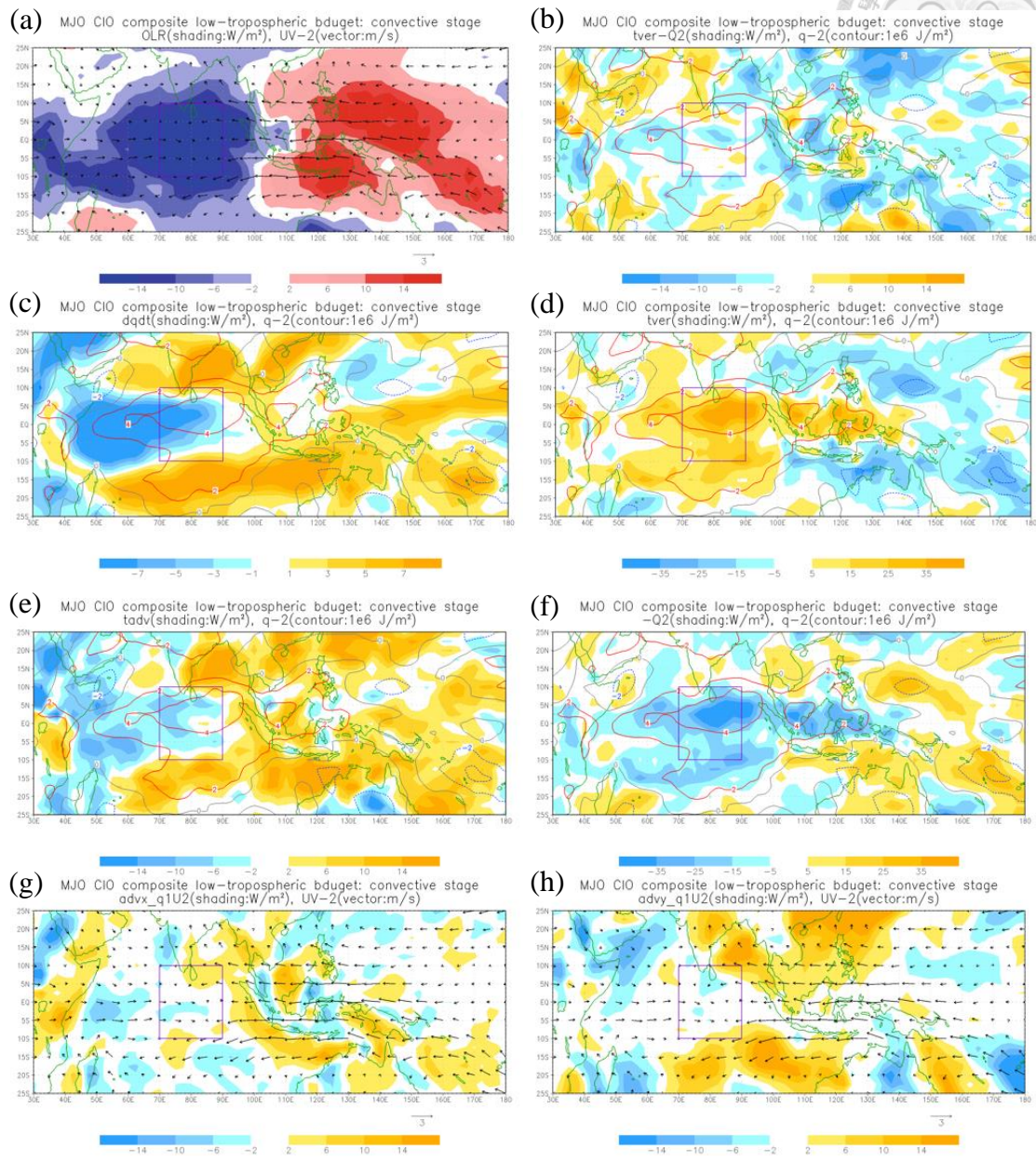
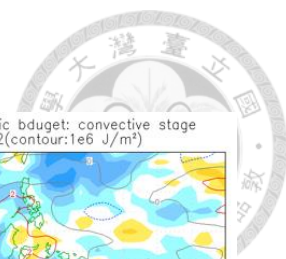


FIG. 19. As in Fig. 17, except for CIO convective stage.

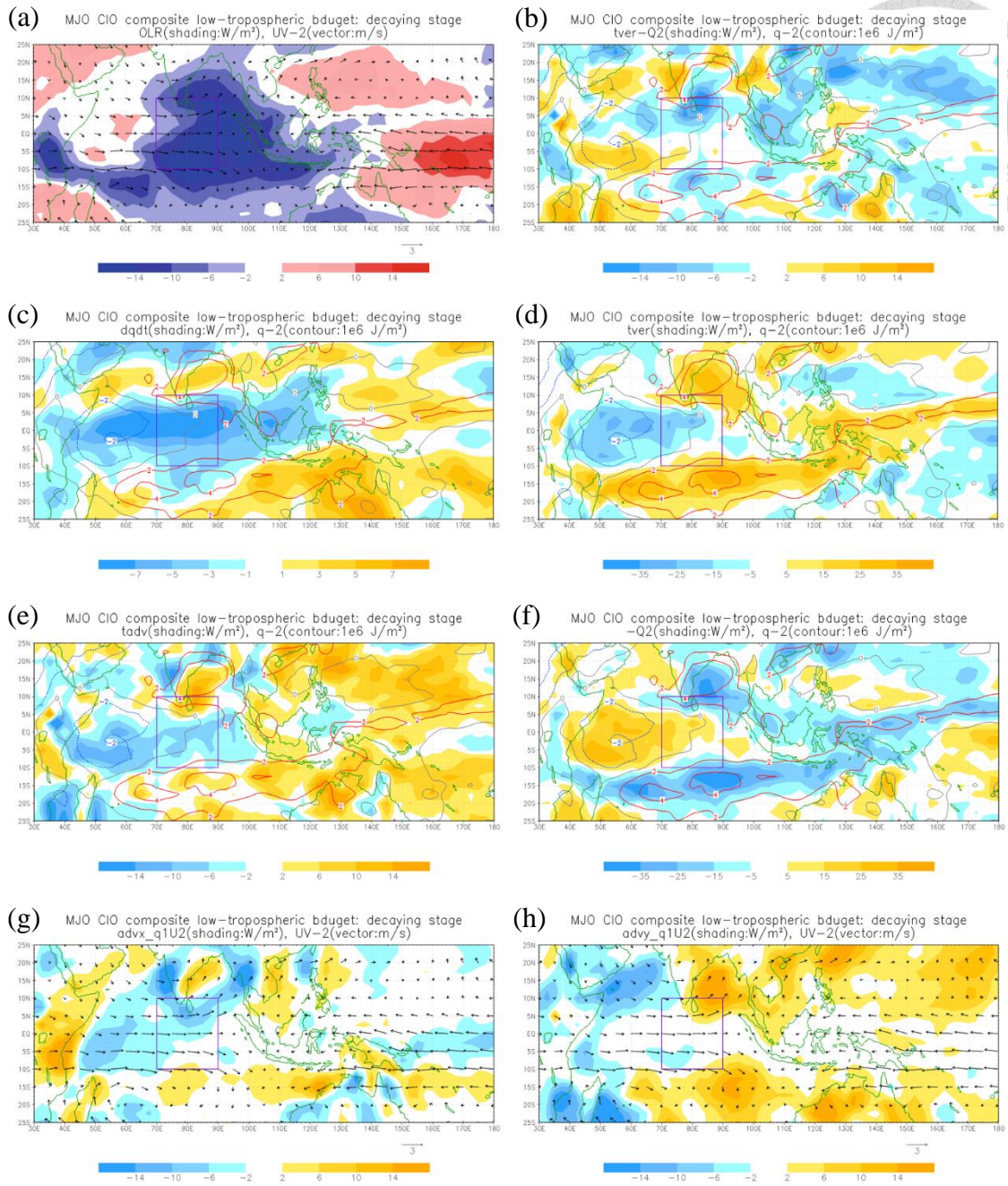


FIG. 20. As in Fig. 17, except for CIO decaying stage.

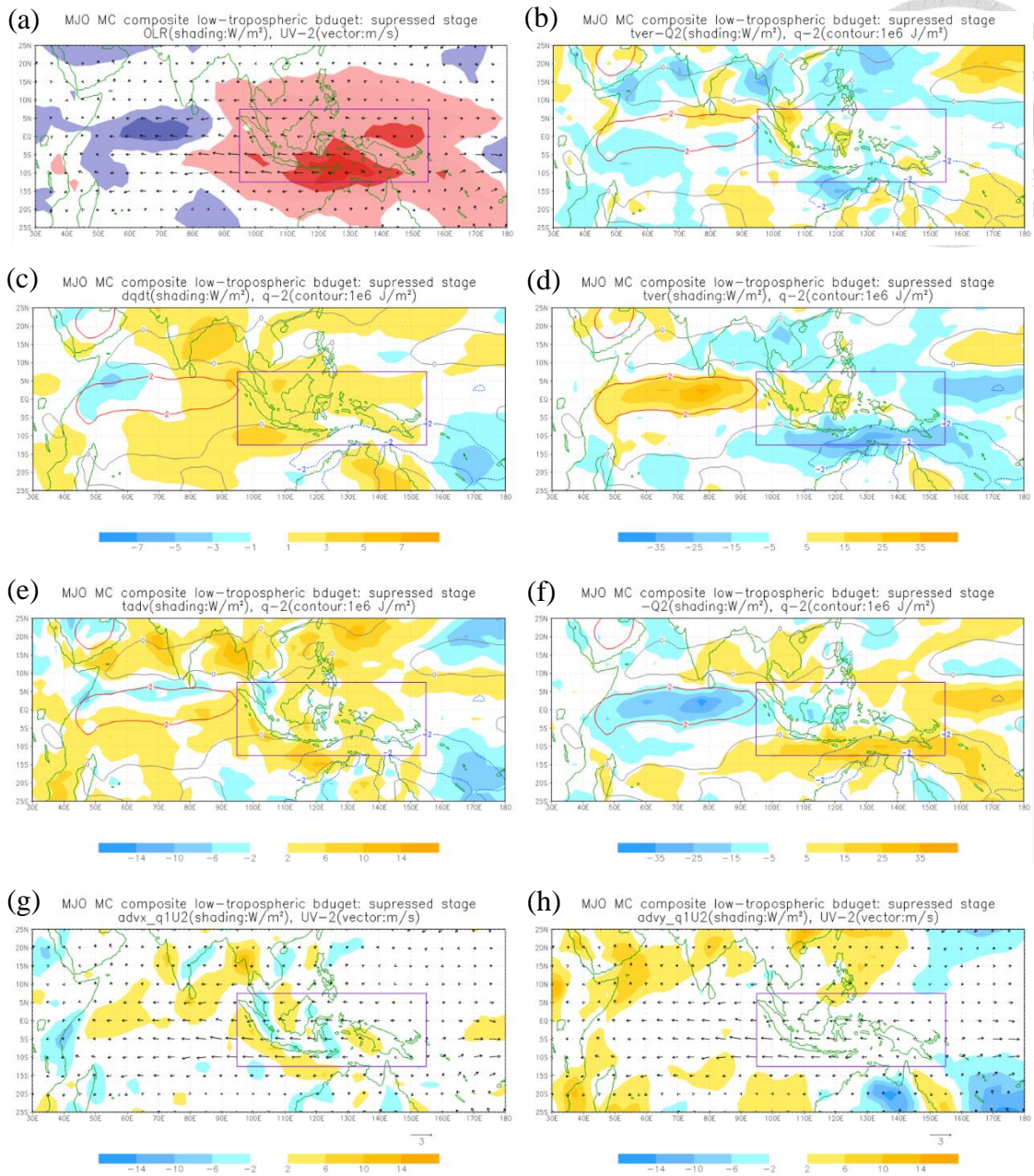


FIG. 21. As in Fig. 17, except for MC suppressed stage.

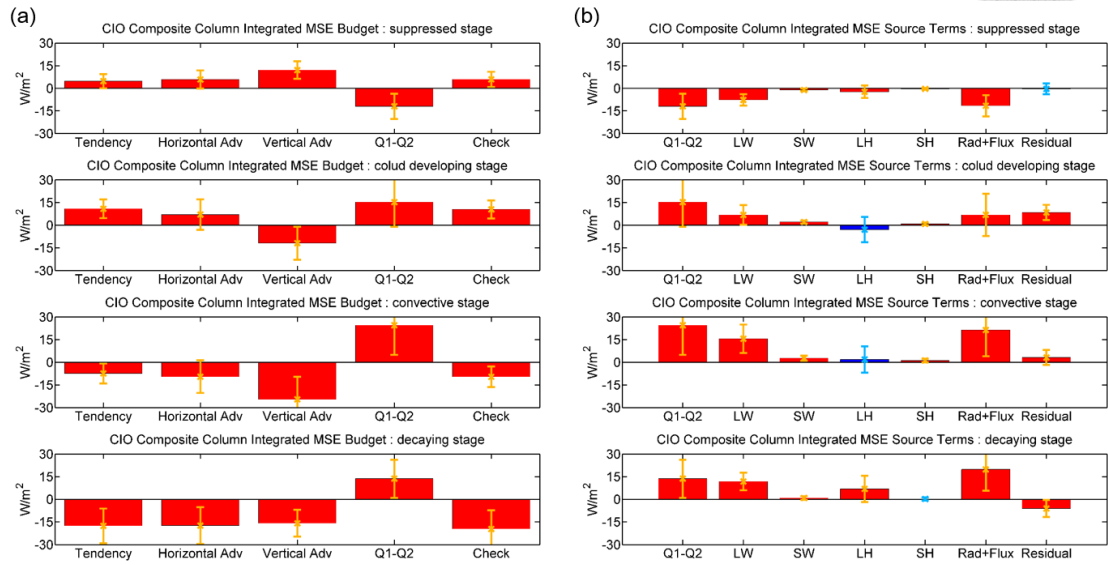


FIG. 22. (a) Column-integrated MSE budget terms and (b) the decomposition of Q_1-Q_2 averaged over four stages. 95% statistically significant budget terms are shown in red. The error bar presents the standard deviation of each term.

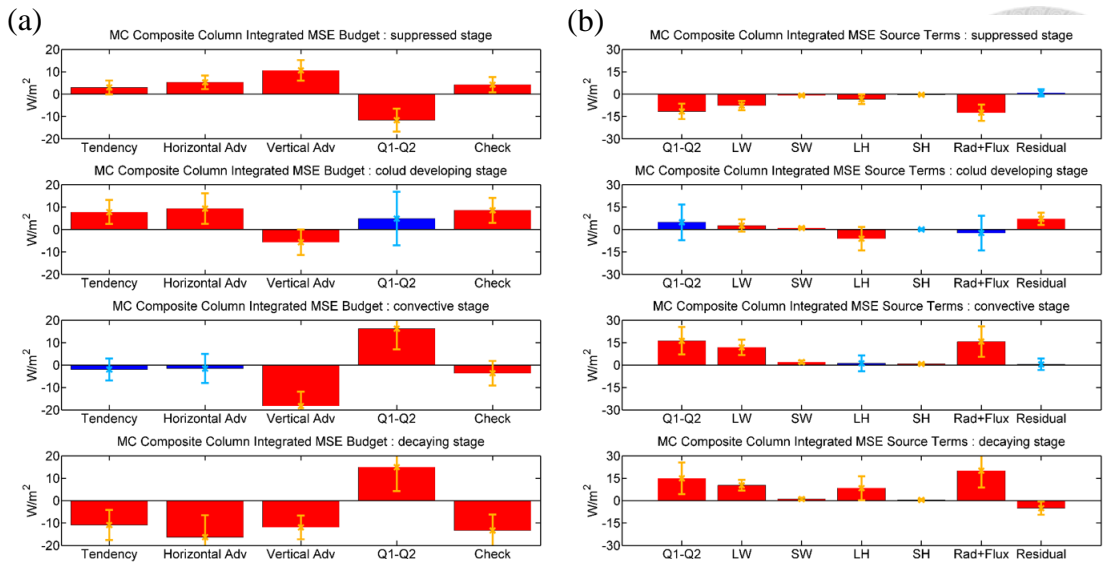


FIG. 23. As in Fig. 22, except for Maritime Continent.

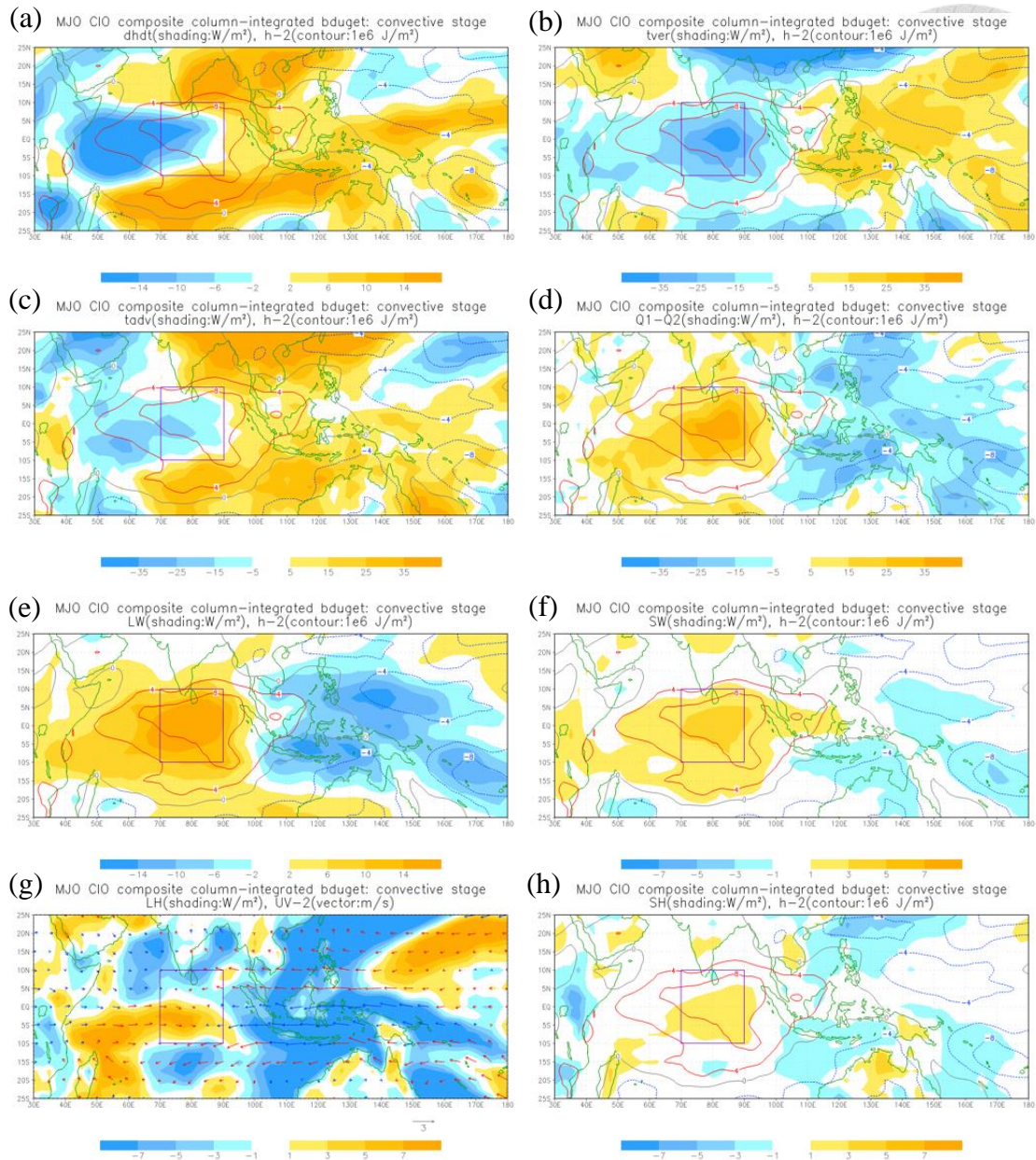



FIG. 24. Horizontal distribution of column-integrated MSE budget terms (shading, W m^{-2}) during the CIO convective stage: (a) tendency, (b) vertical advection, (c) horizontal advection, (d) Q_1-Q_2 . Contoured in each panel is the column-integrated MSE anomaly with interval of 10^6 J m^{-2} . The decomposition of Q_1-Q_2 : (e) longwave radiation, (f) shortwave radiation, (g) latent heat flux, and (h) sensible heat flux. The red (blue) vectors in (g) denote the regions where the intraseasonal flows are in the same (opposite) direction to mean flows.

Appendix

Intercomparison of ISO Indices



Here we compare the statistics of the selected ISO events in section 2c with different ISO indices. For this comparison we use the OLR-based bimodal ISO indices (OBI; Kikuchi et al. 2012), the real-time multivariate MJO index (RMM; Wheeler and Hendon 2004), and the OLR-based MJO index (OMI; Matthews 2008). For all indices, the all-season period of record 1982–2011 is used and the ISO events are selected following the same procedure as depicted in section 2c. The detailed statistics of the selected all-season ISO events are presented in Table A1 and Table A2. The results show that the bimodal ISO indices identify more significant ISO days (Table 1) and select more ISO events (Table 2) than the other two indices, suggesting the use of bimodal ISO indices can capture the seasonal variation of ISO more properly..

Table A1. Number of days for each of the four categories as in Table 1. The number in the brackets shows the ratio to the total number of days (10957 days) during 1982-2011.

	A (Indian Ocean)	B (Maritime Continent)	C (Western Pacific)	D (West Hem. & Africa)	Total
OBI	2232 (20.37%)	1779 (16.24%)	2223 (20.29%)	1917 (17.50%)	8151 (74.39%)
RMM	1669 (15.23%)	1651 (15.07%)	1643 (14.99%)	1686 (15.39%)	6649 (60.68%)
OMI	1602 (14.62%)	1624 (14.82%)	1588 (14.49%)	1495 (13.64%)	6309 (57.58%)

Table A2. Number of instances of the successive and primary events for ISO (left) as in Table 2. Number of consecutive events for ISO (right) as in Table 2. Single means there is no consecutive event (DABCD), double indicates a continuation of two events (DABCDABCD), and so forth.

	Successive (DABCD)	Primary (NABCD)	Quadruple	Triple	Double	Single	Total
OBI	45	13	1	2	4	40	58
RMM	24	18	0	2	5	26	42
OMI	35	15	0	3	7	27	50